Monthly Notices
of the
ROYAL ASTRONOMICAL SOCIETY

MNRAS **493,** 5838–5853 (2020)
Advance Access publication 2020 March 13

doi:10.1093/mnras/staa711

Turbulence in stratified atmospheres: implications for the intracluster medium

Rajsekhar Mohapatra [1]★ Christoph Federrath[1] and Prateek Sharma [2]

[1]*Research School of Astronomy and Astrophysics, Australian National University, Canberra, ACT 2611, Australia*
[2]*Department of Physics, Indian Institute of Science, Bangalore 560012, India*

Accepted 2020 March 10. Received 2020 February 29; in original form 2020 January 16

ABSTRACT

The gas motions in the intracluster medium (ICM) are governed by turbulence. However, since the ICM has a radial profile with the centre being denser than the outskirts, ICM turbulence is stratified. Stratified turbulence is fundamentally different from Kolmogorov (isotropic, homogeneous) turbulence; kinetic energy not only cascades from large to small scales, but it is also converted into buoyancy potential energy. To understand the density and velocity fluctuations in the ICM, we conduct high-resolution ($1024^2 \times 1536$ grid points) hydrodynamical simulations of subsonic turbulence (with rms Mach number $\mathcal{M} \approx 0.25$) and different levels of stratification, quantified by the Richardson number Ri, from Ri = 0 (no stratification) to Ri = 13 (strong stratification). We quantify the density, pressure, and velocity fields for varying stratification because observational studies often use surface brightness fluctuations to infer the turbulent gas velocities of the ICM. We find that the standard deviation of the logarithmic density fluctuations (σ_s), where $s = \ln(\rho/ < \rho(z) >)$, increases with Ri. For weakly stratified subsonic turbulence (Ri $\lesssim$ 10, $\mathcal{M} < 1$), we derive a new σ_s–$\mathcal{M}$–Ri relation, $\sigma_s^2 = \ln(1 + b^2\mathcal{M}^4 + 0.09\mathcal{M}^2 \mathrm{Ri} H_P/H_S)$, where $b = 1/3$–1 is the turbulence driving parameter, and H_P and H_S are the pressure and entropy scale heights, respectively. We further find that the power spectrum of density fluctuations, $P(\rho_k/ < \rho >)$, increases in magnitude with increasing Ri. Its slope in k-space flattens with increasing Ri before steepening again for Ri $\gtrsim$ 1. In contrast to the density spectrum, the velocity power spectrum is invariant to changes in the stratification. Thus, we find that the ratio between density and velocity power spectra strongly depends on Ri, with the total power in density and velocity fluctuations described by our σ_s–$\mathcal{M}$–Ri relation. Pressure fluctuations, on the other hand, are independent of stratification and only depend on $\mathcal{M}$.

Key words: gravitation – hydrodynamics – turbulence – methods: numerical – galaxies: clusters: intracluster medium.

1 INTRODUCTION

An interplay between turbulence and gravity is observed in several terrestrial and astrophysical fluid systems, starting from the earth's atmosphere and oceans to hot ionized plasma in clusters of galaxies (Stein 1967; Mac Low & McCray 1988; Fernando & Hunt 1996; Parmentier, Showman & Lian 2013). All these phenomena are governed by the physics of stratified turbulence. In our study we focus on stratified turbulence in the regimes relevant to the intracluster medium (ICM), which is moderately stratified in the gas density, i.e. the ratio of buoyancy and the turbulent shear forces on the driving scale – defined as the Richardson number (Ri) is $\lesssim$10. Based on their entropy profiles, clusters can be broadly divided into cool cores (CCs) and non-cool cores (NCCs). CC clusters are relaxed with a high (low) central gas density (entropy), and NCCs have large velocity dispersions and are typically undergoing mergers. In Fig. 1, we show the typical Ri profile for these two types of clusters.

Recent observations (Zhuravleva et al. 2014a, 2018; Hitomi Collaboration 2016) have tried to measure turbulent velocities in cluster CCs, which is important to infer details about gas motions and thermodynamics. Hitomi Collaboration measured the gas velocities directly by looking at Doppler line-broadening of Fe xxv and Fe xxvi lines, but such direct measurements will only be available in a few years.[1] We can infer the turbulent velocities indirectly if we can relate them to density fluctuations, which

★ E-mail: rajsekhar.mohapatra@anu.edu.au

[1]https://global.jaxa.jp/projects/sas/xrism/

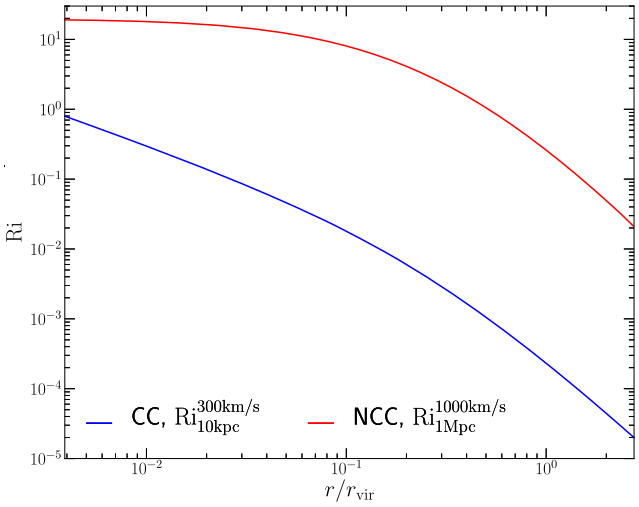

Figure 1. Typical Ri profiles for CC and NCC clusters. We calculate Ri using the driving length-scale $L_{\rm driv}$ and the turbulent velocity on scale $L_{\rm driv}$, $v_{L_{\rm driv}}$, indicated in the subscripts and superscripts in the legends, respectively. For CC clusters, we consider driving by AGN jets with $L_{\rm driv} \approx 10$ kpc and $v_{L_{\rm driv}} \approx 300\ \mathrm{km\,s^{-1}}$ (Hitomi Collaboration 2016). For NCC clusters, we consider driving by mergers with $L_{\rm driv} \approx 1$ Mpc and $v_{L_{\rm driv}} \approx 1000\ \mathrm{km\,s^{-1}}$. Here, we use the Brunt–Vaisala frequency N from fig. 1 in Shi & Zhang (2019). Note that $\mathrm{Ri} = N^2 L^2_{\rm driv}/v^2_{L_{\rm driv}}$ is sensitive to the choice of $L_{\rm driv}$ and $v_{L_{\rm driv}}$. Moderately stratified turbulence with $\mathrm{Ri} \lesssim 10$ governs both CC and NCC clusters.

are easier to measure from X-ray surface brightness (SB) maps (e.g. Zhuravleva et al. 2014a). Other than CCs, on larger scales such as cluster outskirts, turbulent pressure is a key component of the non-thermal pressure support. Estimating turbulent velocities is again important in calculating the hydrostatic mass bias of clusters (Schuecker et al. 2004; Bautz et al. 2009; George et al. 2009; Cavaliere, Lapi & Fusco-Femiano 2011; Nelson, Lau & Nagai 2014). On these scales, pressure fluctuations obtained from Sunyaev–Zeldovich effect (SZ) observations can also be used to estimate gas velocities (Zeldovich & Sunyaev 1969; Khatri & Gaspari 2016; Mroczkowski et al. 2019). Thus, a detailed study of density, pressure, and velocity fluctuations in a stratified medium is important to obtain reliable scaling relations between different observables and velocities (see Simionescu et al. 2019 for a review on ICM gas velocities).

Many current turbulence studies of the ICM typically ignore the effects of gravity (and hence stratification), and model it using homogeneous isotropic turbulence (Brunetti & Lazarian 2007; Banerjee & Sharma 2014; Mohapatra & Sharma 2019; Grete, O'Shea & Beckwith 2020). However, the gas distribution in the ICM is neither homogeneous nor isotropic. Instead, the density distribution is stratified and is in rough hydrostatic equilibrium with the gravitational profile. Stratified turbulence itself is fundamentally different from homogeneous isotropic turbulence, in that it opens up a new channel of energy exchange. While in homogeneous isotropic turbulence, kinetic energy cascades down through eddies of decreasing sizes and is ultimately dissipated on the viscous length-scale (Frisch 1995), in stratified turbulence energy can also be channelled back and forth between kinetic energy and gravitational potential energy (Bolgiano 1962; Verma 2018). Due to these fundamental differences ϵ_ℓ, the rate of transfer of kinetic energy on length-scale ℓ can vary as a function of ℓ. This can change the interpretation of important statistical tools used to analyse turbulence, such as velocity and density distributions, power spectra of velocity and density and their correlation functions.

In most current theoretical and computational studies of stratified turbulence, driving is generally perpendicular to the direction of gravity (Carnevale, Briscolini & Orlandi 2001; Lindborg 2006; Brethouwer & Lindborg 2008; Herring & Kimura 2013; Kumar, Chatterjee & Verma 2014). They are designed to model stratified turbulence in planetary atmosphere and oceans. However, turbulence in the cluster cores is driven more isotropically by active galactic nuclei (AGNs) jets and gravitational mergers (Balbus & Soker 1990; Churazov et al. 2002, 2003; Omma et al. 2004; Nelson et al. 2012). Also, to obtain scaling relations between density and velocity fluctuations, we need to scan a larger parameter space of Ri than what has been done in current studies. We therefore drive turbulence isotropically in a local idealized model of a cluster atmosphere. We present scaling relations between density, pressure, and velocity fluctuations to understand stratified turbulence through our simulations.

Recent ICM turbulence studies such as Gaspari, Ruszkowski & Sharma (2012), Zhuravleva et al. (2014b), Zhang, Churazov & Schekochihin (2018), Valdarnini (2019), and Shi & Zhang (2019) include gravitational stratification in their models. However, these simulations mostly cannot resolve the Ozmidov length $l_{\rm O}$ (the length-scale where turbulent shear and stratification terms are equal in magnitude) within the inertial range of turbulence. Even in high-resolution simulations where $l_{\rm O}$ is resolved, there is a lack of a detailed study of how turbulence varies with the changing strength of stratification in clusters as parametrized by Ri.

In this study, we analyse turbulence by varying the stratification strength in the parameter space relevant to the ICM (i.e. $0.001 \lesssim \mathrm{Ri} \lesssim 10$, see Table 1) and compare some key turbulence statistics (such as probability distribution functions (PDFs) of velocity, density, power spectra of density and velocity). We resolve $l_{\rm O}$ in the inertial range of our simulations.

The paper is organized as follows: in Section 2, we describe our setup and methods, we present our results and their interpretations in Section 3, we compare our results with the literature and discuss the caveats of our work in Section 4, and we conclude in Section 5.

2 METHODS

2.1 Model equations

We model the ICM using hydrodynamic equations with gravity and turbulent forcing as additional source terms in the momentum and energy equations. We solve the following equations:

$$\frac{\partial \rho}{\partial t} + \nabla \cdot (\rho \mathbf{v}) = 0, \tag{1a}$$

$$\frac{\partial (\rho \mathbf{v})}{\partial t} + \nabla \cdot (\rho \mathbf{v} \otimes \mathbf{v}) + \nabla P = \rho \mathbf{F} + \rho \mathbf{g}, \tag{1b}$$

$$\frac{\partial E}{\partial t} + \nabla \cdot ((E + P)\mathbf{v}) = \rho \mathbf{F} \cdot \mathbf{v} + \rho (\mathbf{v} \cdot \nabla)\Phi, \tag{1c}$$

where ρ is the gas mass density, $\mathbf{v}$ is the velocity, $P = \rho k_{\rm B} T/(\mu m_{\rm p})$ is the pressure (we use the ideal gas equation of state), $\mathbf{F}$ is the turbulent acceleration that we apply, Φ is the gravitational potential, $\mathbf{g} = -\nabla\Phi$ is the acceleration due to gravity, $E = \rho v^2/2 + P/(\gamma - 1)$ is the sum of kinetic and internal energy densities, μ is the mean particle weight, $m_{\rm p}$ is the proton mass, $k_{\rm B}$ is the Boltzmann constant, T is the temperature, and $\gamma = 5/3$ is the adiabatic index. We assume that the gas is fully ionized with a third solar metallicity (which is the case for typical ICM conditions) and this gives us $\mu \approx 0.61$.

Table 1. Simulation parameters for different runs.

Label (1)	Ri (2)	H_ρ (3)	H_P (4)	Resolution (5)	$\mathcal{M}$ (6)	σ_s (7)	α (8)
Ri0.05LowRes	0.05 ± 0.02	3.0	6.0	$512^2 \times 768$	0.254 ± 0.008	0.035 ± 0.005	-1.71 ± 0.06
Ri0	0	∞	∞	$1024^2 \times 1536$	0.26 ± 0.01	0.021 ± 0.001	-2.06 ± 0.01
Ri0.003	0.003 ± 0.001	15.0	30.0	$1024^2 \times 1536$	0.26 ± 0.01	0.022 ± 0.001	-1.99 ± 0.02
Ri0.01	0.012 ± 0.003	6.0	12.0	$1024^2 \times 1536$	0.256 ± 0.002	0.026 ± 0.002	-1.96 ± 0.02
Ri0.05	0.05 ± 0.02	3.0	6.0	$1024^2 \times 1536$	0.258 ± 0.007	0.037 ± 0.003	-1.86 ± 0.02
Ri0.2	0.24 ± 0.06	1.5	3.0	$1024^2 \times 1536$	0.25 ± 0.01	0.06 ± 0.01	-1.79 ± 0.03
Ri0.5	0.5 ± 0.1	1.0	2.0	$1024^2 \times 1536$	0.25 ± 0.02	0.08 ± 0.01	-1.77 ± 0.04
Ri0.6NV	0.6 ± 0.2	1.0	2.0	$1024^2 \times 1536$	0.25 ± 0.01	0.07 ± 0.01	-1.77 ± 0.03
Ri1	1.0 ± 0.3	0.75	1.5	$1024^2 \times 1536$	0.25 ± 0.01	0.10 ± 0.02	-1.77 ± 0.03
Ri3	3.0 ± 1.0	0.5	1.0	$1024^2 \times 1536$	0.25 ± 0.01	0.14 ± 0.01	-1.83 ± 0.03
Ri13	13^{-6}_{+11}	0.25	0.5	$1024^2 \times 1536$	0.26 ± 0.02	0.20 ± 0.02	-1.91 ± 0.01
Ri10NV	9^{-4}_{+7}	0.25	0.5	$1024^2 \times 1536$	0.30 ± 0.01	0.22 ± 0.02	-1.88 ± 0.02
Ri0.05HighRes	0.05 ± 0.02	3.0	6.0	$2048^2 \times 3072$	0.257 ± 0.007	0.037 ± 0.003	-1.86 ± 0.01

Note. Column 1 shows the simulation name. The number following 'Ri' is the average Richardson number in the simulation. The default resolution of all runs is $1024^2 \times 1536$, 'LowRes' refers to $512^2 \times 768$, and 'HighRes' to $2048^2 \times 3072$. 'NV' stands for turbulent forcing only in the directions perpendicular to gravity. In columns 2–4, we list Ri, H_ρ, and H_P, which are simulation parameters defined in equations (8), (2a), and (2b). Column 5 lists the grid resolution. In column 8, $\mathcal{M}$ refers to the rms Mach number (see equation 9c). Column 7 shows σ_s, the standard deviation of s (defined in equation 9d). In column 8, α refers to the spectral slope of $P(\bar{\rho}_k)$, the power spectrum of normalized density fluctuations. We have defined the normalization of density fluctuations in equation (9a). All quantities ($\mathcal{M}, \alpha, \sigma_\mathrm{s}$) were averaged over five turbulent turnover times, for $3 \leq t/t_\mathrm{turb} \leq 8$.

2.2 Setup

We choose $-\hat{\mathbf{z}}$ to be the direction of the gravitational field, and pressure and density to have scale heights H_P and H_ρ, respectively. Thus, the initial pressure and density profiles are given by

$$P(t=0) = P_0 \exp\left(-\frac{z}{H_\mathrm{P}}\right) \text{ and} \tag{2a}$$

$$\rho(t=0) = \rho_0 \exp\left(-\frac{z}{H_\rho}\right), \text{ respectively.} \tag{2b}$$

Since we start with the gas in hydrostatic equilibrium, the initial density and pressure are related by

$$\frac{\mathrm{d}P}{\mathrm{d}z} = -\rho g. \tag{3a}$$

Hence, g is set as

$$g = \frac{P_0}{\rho_0 H_\mathrm{P}} \exp\left(-z\left[\frac{1}{H_\mathrm{P}} - \frac{1}{H_\rho}\right]\right). \tag{3b}$$

This equilibrium is convectively stable if $\mathrm{d}\ln S/\mathrm{d}z > 0$, where

$$S = \frac{P}{\rho^\gamma} \text{ is the pseudo-entropy.} \tag{4}$$

This gives us the condition for the entropy scale height H_S ($\equiv 1/[\mathrm{d}\ln S/\mathrm{d}z]$)

$$\frac{1}{H_\mathrm{S}} = \frac{\gamma}{H_\rho} - \frac{1}{H_\mathrm{P}} > 0. \tag{5}$$

This condition is satisfied for all our simulations, which locally mimic the stably stratified ICM.

2.3 Calculating the Richardson number (Ri)

Consider a parcel of gas with density ρ' and pressure P' at $z = z$, moving with $v_z > 0$. As the parcel rises subsonically to $z + \delta z$, it is in pressure equilibrium with its surroundings, but does not exchange energy with it. Thus the gas parcel is adiabatic. The Lagrangian changes in the pressure and density of the parcel, respectively, are

$$\Delta P' = P'(z+\delta z) - P'(z) = \frac{\mathrm{d}P'}{\mathrm{d}z}\delta z, \tag{6a}$$

$$\Delta\rho' = \left(\frac{\partial\rho'}{\partial P'}\right)_\mathrm{S} \Delta P'. \tag{6b}$$

Since the ambient density $\rho(z)$ itself changes as a function of z, the Eulerian overdensity at $z + \delta z$ is given by

$$\delta\rho = \frac{\mathrm{d}P}{\mathrm{d}z}\left[\left(\frac{\partial\rho'}{\partial P'}\right)_\mathrm{S} - \frac{\mathrm{d}\rho}{\mathrm{d}P}\right]\delta z. \tag{6c}$$

The quantity inside the square brackets should be positive for a stable stratification. The buoyancy acceleration acting on the displaced parcel is $\delta\rho' g/\rho$ and the equation of motion for the gas parcel is

$$\frac{\mathrm{d}^2\delta z}{\mathrm{d}t^2} = -\underbrace{\frac{g}{\gamma}\frac{d}{dz}\ln\left(\frac{P}{\rho^\gamma}\right)}_{N^2}\delta z = -N^2\delta z, \tag{6d}$$

where N^2 is the square of the Brunt–Vaisala (BV) frequency. The condition for stable stratification is $N^2 > 0$, or

$$\left(\frac{\gamma}{H_\rho} - \frac{1}{H_\mathrm{P}}\right) > 0, \text{ or } H_\rho/H_\mathrm{P} < \gamma, \tag{7}$$

as mentioned earlier.

The scale-dependent turbulent Richardson number Ri_ℓ at a length-scale ℓ is defined as

$$\mathrm{Ri}_\ell = \frac{N^2}{(v_\ell/\ell)^2}, \tag{8}$$

where v_ℓ is the velocity on length-scale ℓ. On large scales, stratification is expected to be dominant over turbulence so we can have $\mathrm{Ri}_\ell > 1$, while on small enough length-scales, turbulence dominates to give $\mathrm{Ri}_\ell < 1$. The length-scale on which $\mathrm{Ri}_\ell = 1$ is called the Ozmidov length-scale l_O ($\mathrm{Ri}_{l_\mathrm{O}} = 1$).

Table 1 shows the different choices of H_ρ and H_P for different simulations and the Richardson number $\mathrm{Ri}_{L_\mathrm{driv}}$ on the driving

scale $L_{\rm driv}$, which we shall refer to as Ri from now on. An equivalent dimensionless number, the Froude number ($\mathrm{Fr} = \mathrm{Ri}^{-1/2}$) is sometimes used to describe turbulence in stratified fluids.

2.4 Normalization

In order to compare density, pressure, and velocity fluctuations in stably stratified turbulence, we first normalize these fluctuations to construct dimensionless variables $\bar{\rho}$, $\bar{P}$, and $\mathcal{M}$ and s. These variables are given by

$$\bar{\rho} = \frac{\rho}{\langle \rho(z) \rangle}, \tag{9a}$$

$$\bar{P} = \frac{P}{\langle P(z) \rangle}, \tag{9b}$$

$$\mathcal{M} = \left\langle \frac{v}{c_{\rm s}} \right\rangle_{\rm rms}, \text{ and} \tag{9c}$$

$$s = \ln(\bar{\rho}), \tag{9d}$$

where $<\rho(z)>$ and $<P(z)>$ are the average density and pressure at $z = z$ slice, respectively, v is the amplitude of velocity and c_s is the local speed of sound.

2.5 Calculating the potential energy ($E_{u_{\rm b}}$)

Equation (6d) shows that a gas parcel experiences a restoring force when displaced in the vertical direction. In the absence of continuous turbulence driving, this parcel would oscillate about its mean position like a harmonic oscillator with a natural frequency N (chapter 4, Lighthill 1978). The potential energy (per unit mass) is thus given by

$$N^2 \delta z^2/2 = g^2(\delta\rho/\rho)^2/2N^2, \tag{10}$$

using equations (6c) and (6d). We define a quantity $u_{\rm b} = g\delta\bar{\rho}/N$ with dimensions of velocity. The potential energy per unit mass is given by

$$E_{u_{\rm b}} = u_{\rm b}^2/2. \tag{11}$$

On substituting the expressions for g and N from equations (3b) and (6d) for the two profiles, we obtain

$$E_{u_{\rm b}} = \frac{\rm P}{2\rho} \frac{\delta\bar{\rho}^2}{\frac{H_{\rm P}}{H_\rho} - \frac{1}{\gamma}}. \tag{12}$$

As usual, the fluctuating kinetic energy per unit mass is $E_{\rm u} = \delta v^2/2$, where δv is the magnitude of the fluctuating velocity at a given height.

2.6 Numerical methods

We use a modified version of the FLASH code (Fryxell et al. 2000; Dubey et al. 2008), version 4, for our simulations. We evolve the Euler equations in FLASH, with additional gravity and forcing terms in the momentum and energy equations (1a–c). The pressure, density, and temperature of the gas are related by the ideal gas equation of state. We use the hydrodynamic version of the HLL3R Riemann solver (Bouchut, Klingenberg & Waagan 2007, 2010) to solve the Euler equations. This solver has been tested for efficiency, robustness, and accuracy in Waagan, Federrath & Klingenberg (2011). We use a uniformly spaced 3D grid, with periodic boundary conditions along the x- and y-directions. In the z-direction, we use reflective boundary conditions. We work with dimensionless units, such that density (ρ_0) and initial speed of sound ($c_{\rm s,\,0}$) at $z = 0$ are unity (refer to equations 2a and b for definitions). We set the box size along x and y to be $L_x = L_y = 1$. In order to minimize any anomalous effects of the reflective boundary conditions, we use a larger box size along the z-direction, $L_z = 1.5$. However, we analyse the simulations only inside the cube of size $L = 1$ centred at (0,0,0). Thus, the boundaries of our analysis box are at ($\pm$ 0.5, $\pm$0.5, $\pm$0.5). Our simulations have a maximum grid resolution of $2048^2 \times 3072$ (with most runs being $1024^2 \times 1536$), the larger number of cells being in the z-direction, so that the individual cells are cubical. We have checked our results for convergence over different resolutions ($512^2 \times 768$, $1024^2 \times 1536$, and $2048^2 \times 3072$) in Figs A1 and A2. We have confirmed that any effects of our choice of boundary conditions and box size along the z-direction are minimal, by testing other boundary conditions and different box sizes along the z-direction.

2.7 Turbulent forcing

We follow a spectral forcing method using the stochastic Ornstein–Uhlenbeck (OU) process to model the turbulent acceleration $\mathbf{F}$ with a finite autocorrelation time-scale $t_{\rm turb}$ (Eswaran & Pope 1988; Schmidt, Hillebrandt & Niemeyer 2006; Federrath et al. 2010). The acceleration $\mathbf{F}$ only contains large-scale modes, $1 \leq |\mathbf{k}|L/2\pi \leq 3$. The power injected is a parabolic function of $|\mathbf{k}|$ and peaks at the $k_{\rm inj} = 2$ mode in Fourier space, i.e. on half of the box size (for simplicity, we have dropped the wavenumber unit $2\pi/L$ in the rest of the paper). Turbulence on scales $k \geq 3$ develops self-consistently, and is not directly driven. We set the autocorrelation time-scale on the driving scale, $t_{\rm turb} = (L/2)/\sigma_v$, where σ_v is the standard deviation of velocity on the driving scale, $L/2$. Our driving is solenoidal, i.e. the acceleration field has zero divergence and non-zero curl. Compressive forcing can give rise to larger density perturbations (Federrath, Klessen & Schmidt 2008), which we do not include in this study. We use the same forcing field for all of our simulations. For further details of the forcing method, refer to section 2.1 of Federrath et al. (2010).

To minimize any anomalous effects of the reflective boundary conditions in the z- direction, we apply a window function on the turbulence acceleration field. This window function slowly decays the external acceleration amplitude to zero close to the reflective boundaries in the z-direction (for all three components of acceleration). The window function is given by

$$w(z) = 1 \text{ for } |z| < 0.625,$$
$$= \exp(-||z| - 0.625|/0.125) \text{ for } |z| > 0.625. \tag{13}$$

Note that $w(z) = 1$ inside the analysis box. Thus, the driving amplitude is reduced exponentially, only very close to the computational domain boundaries in z.

2.8 Relevance to the ICM

Although we work with dimensionless units, our results can easily be scaled to model the ICM. If we take $L = 40\,\mathrm{kpc}$, Then the driving scale ranges between 10 and 20 kpc. If the sound speed $c_{\rm s} \approx 500\ \mathrm{km\,s^{-1}}$, then with $\mathcal{M} \approx 0.25$, $v_{\rm turb} \approx 125\ \mathrm{km\,s^{-1}}$. The gas temperature profile is given by

$$T = T_0 \exp\left(-z\left[\frac{1}{H_{\rm P}} - \frac{1}{H_\rho}\right]\right), \tag{14}$$

where $T_0 \approx 1\mathrm{keV}$. The scale height of density H_ρ varies between 10 and 600 kpc and $H_{\rm P} = 2H_\rho$ for various runs. For modelling galaxy

clusters, we choose $H_P > H_\rho$ such that T increases with increasing z. Although the temperature decreases with radius in NCCs, our results are applicable there too because the buoyant response depends on the entropy gradient rather than the temperature gradient. In the presence of thermal conduction (both isotropic and anisotropic), the physics of stratified turbulence is modified, and temperature fluctuations and gradients become important (McCourt et al. 2011; Gaspari et al. 2014). This investigation is beyond the scope of this paper.

3 RESULTS AND DISCUSSION

Here, we describe the results of our simulations and discuss their possible implications in the context of clusters, and stratified turbulence in general. Table 1 lists the different simulation parameters for our runs. We use an identical acceleration field to drive turbulence in all our simulations. Thus, all our simulations have approximately the same subsonic $\mathcal{M} \approx 0.25$ in steady state. We run the simulations for a total of 8 eddy turnover times ($t_{\rm eddy} = t_{\rm turb}$) on the driving scale. We have chosen a standard set of runs – Ri0, Ri0.003, Ri0.05, Ri0.2, Ri1.0, and Ri13 (Ri denoted by the number in the label) for our analysis.

Fig. 2 shows the time evolution of $\mathcal{M}$, σ_s, E_{u_b} and E_{u_z} (σ_s in standard deviation in s over the entire analysis cube). All these quantities reach a steady state at around $t = 3\,t_{\rm turb}$. Thus, we start analysing turbulence at this time and we have a total duration of $5\,t_{\rm turb}$ for statistical averaging (from $3\,t_{\rm turb}$ to $8\,t_{\rm turb}$). The gas only heats up slightly due to viscous dissipation of energy, increasing the sound speed with time. However, this change is not significant ($\lesssim 10$ per cent) and $\mathcal{M}$ roughly remains constant for the entire duration of the analysis and statistical averaging, as shown in the top panel of Fig. 2.

3.1 Evolution of density perturbations and potential and kinetic energies

X-ray SB fluctuations are used to calculate density perturbations in the ICM, and these are further used to constrain turbulent gas velocities (Zhuravleva et al. 2014b). Turbulence alone can produce density fluctuations (e.g. Passot & Vázquez-Semadeni 1998; Federrath et al. 2008). However, with stratification, turbulence gives rise to a new kind of density perturbations. When a parcel of gas moves to higher (lower) z, it has higher (lower) density compared to the local profile and appears as positive (negative) density perturbation at the parcel's new location. For unstratified subsonic turbulence, the density perturbations are much smaller and increase roughly quadratically with the Mach number (Mohapatra & Sharma 2019).

The second panel of Fig. 2 shows that the amplitude of density fluctuations σ_s increases with increasing strength of the stratification. For Ri $\gtrsim 0.05$, these buoyancy-induced density fluctuations are larger than the density fluctuations produced by unstratified turbulence, as seen in effectively unstratified turbulence runs with Ri $= 0$ and 0.003. Column 7 of Table 1 lists σ_s for different runs. We discuss more about σ_s and Ri in Section 3.5.

The vertical motions of parcels of gas also convert z-direction kinetic energy into gravitational potential energy due to work done against the buoyancy force. This mechanism of energy transfer is absent in unstratified turbulence. The third and fourth panels of Fig. 2 show that E_{u_b} increases and E_{u_z} decreases and the ratio E_{u_b}/E_{u_z} increases with increasing stratification, as more and more of the driven energy is converted into potential energy. An increasing potential energy with increasing Ri is expected from a simple model of a driven-damped harmonic oscillator.

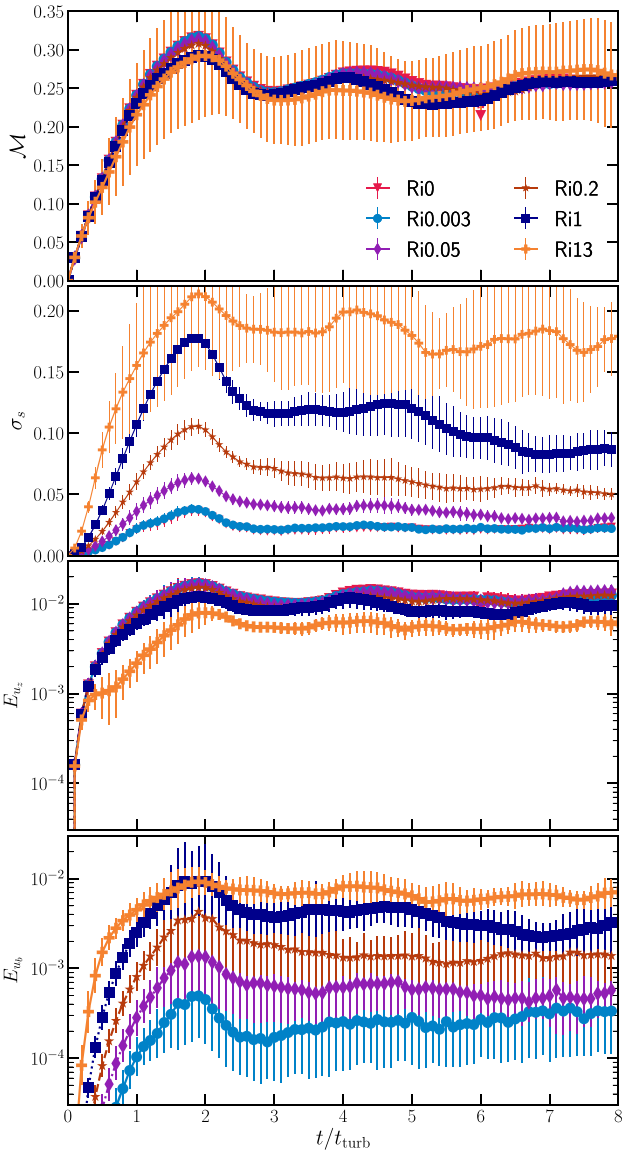

Figure 2. Time evolution of (first panel $\mathcal{M}$) rms Mach number, (second panel σ_s) logarithmic density fluctuations, (third panel E_{u_z}) specific kinetic energy in z-direction, and (fourth panel E_{u_b}) specific potential energy for the standard set of runs (Ri0, Ri0.003, Ri0.05, Ri0.2, Ri1.0, and Ri13). The errorbars indicate the standard deviation of these quantities after averaging them in constant z slices. In steady state, $\mathcal{M} \approx 0.25$ is similar for all runs, σ_s and E_{u_b} increase, while E_{u_z} decreases (significantly for Ri $\gtrsim 1$) with increasing stratification.

3.2 Volume and column density structure

Here, we present mock observables such as column density (similar to X-ray SB if density fluctuations are small as in this case) and the relative fluctuations thereof. We also plot density slices to look into the effect of integrating along the line of sight (LOS) and superimpose the corresponding velocity field.

The left-hand panel of Fig. 3 shows the density and velocity fields integrated perpendicular to the stratification direction (along

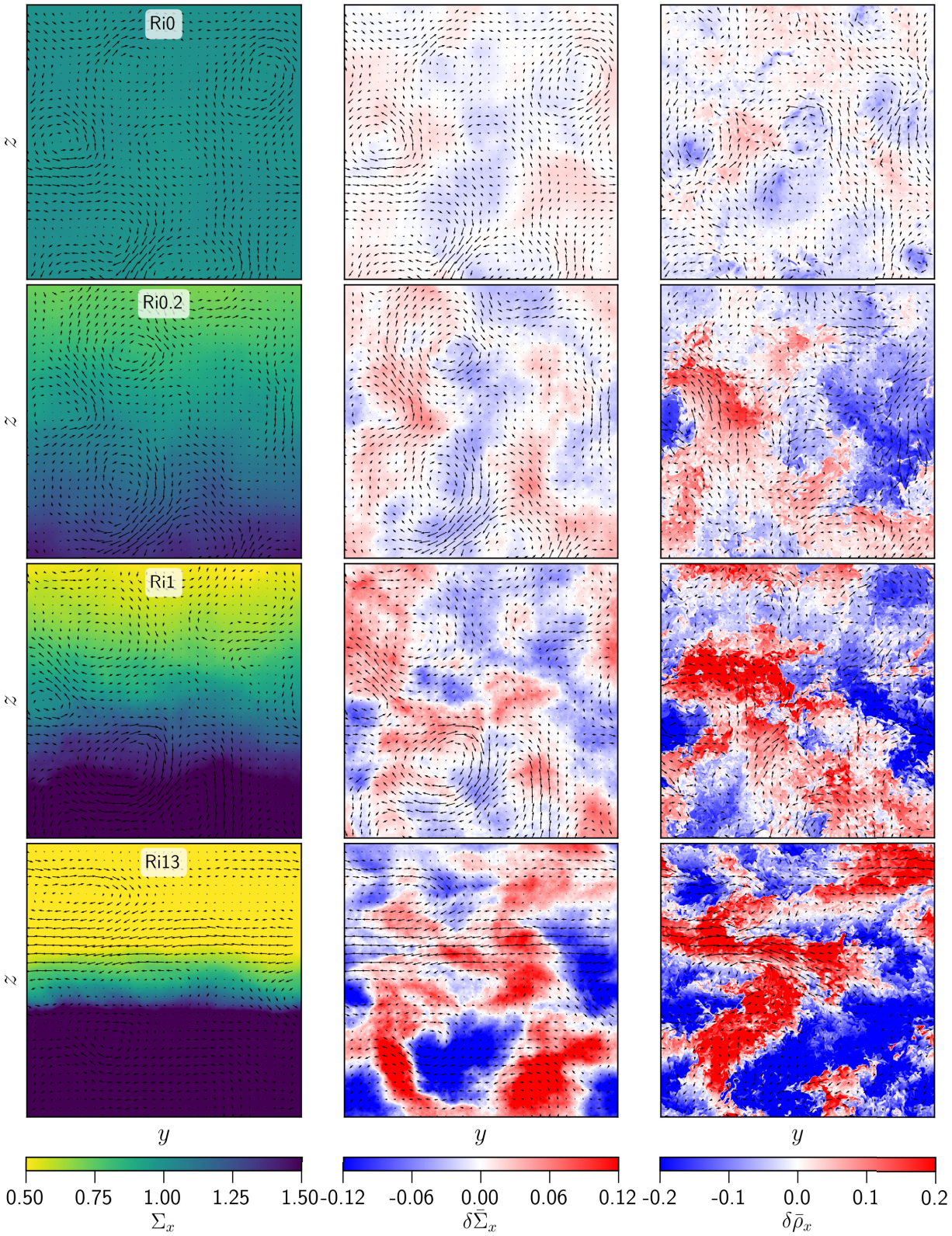

Figure 3. *First column:* Σ_x, the density projection along x (perpendicular to the stratification direction), for runs Ri0, Ri0.2, Ri1, and Ri13 at $t = 6\,t_{\rm turb}$. The arrows indicate the integrated velocity field in the yz-plane. The density gradient along z is stronger for stronger stratification. *Second column:* Corresponding $\bar{\Sigma}_x$ perturbations $\delta\bar{\Sigma}_x$ for different runs. These are obtained by dividing the observed density snapshot by the average density profile for that time and subtracting 1 from it. Column density perturbations are significantly stronger for stronger stratification runs. *Third column:* Normalized density perturbation slices $\delta\bar{\rho}_x$ taken in $x = 0$ plane. These plots show more small-scale features and are of larger amplitude than $\delta\bar{\Sigma}_x$.

x-direction, for simulations Ri0, Ri0.2, Ri1, and Ri13 (from top to bottom), i.e. from pure turbulence (top) to strong stratification (bottom), at $t = 6\,t_{\rm turb}$. We denote column density and column density fluctuations (normalized with respect to the stratification profile) by Σ_i and $\delta\bar{\Sigma}_i$ respectively, where $\Sigma_i = \int \rho {\rm d}i$ and $\delta\bar{\Sigma}_i = \int \bar{\rho}{\rm d}i - 1$, with i denoting the LOS direction. These Σ_i and $\delta\bar{\Sigma}_i$ plots provide a sense of comparison between the 3D structure of the ICM and the X-ray SB observations. For x as the LOS direction, the SB of ICM gas is proportional to $\int \rho^2 {\rm d}x$. The SB fluctuations $\delta\bar{\rm SB}$ for small density fluctuations ($\delta\rho/\rho_0 < 1$) are then proportional to $\int 2\rho_0^2 \delta\bar{\rho}{\rm d}x \approx 2\rho_0^2 \delta\bar{\Sigma}_x$.

We look for possible correlations between these mock observables and their dependence on Ri. From the middle panel of Fig. 3, we find that $\delta\bar{\Sigma}_x$ increases with increasing Ri. This is what we expect, since $\sigma_{\rm s}$ increases with Ri (second panel, Fig. 2).

Density slices (normalized with respect to the stratification profile) parallel to the i-axis passing through the origin are denoted by $\bar{\rho}_i$ and perturbation slices by $\delta\bar{\rho}_i$ ($\bar{\rho}_i = \bar{\rho}|_{i=i}, \delta\bar{\rho}_i = (\bar{\rho} - 1)|_{i=i}$). The density fluctuations $\delta\bar{\rho}_i$ for different runs are plotted in the right-hand panels of Fig. 3. We find that $\delta\bar{\rho}_x$ also increases with increasing Ri. We see more small-scale structures in $\delta\bar{\rho}_x$ which disappear in $\delta\bar{\Sigma}_x$ due to integration along the x-direction.

For Ri $\gg 1$ (bottom panel, Fig. 3), the velocity field becomes primarily horizontal, the eddies become shorter in the vertical direction, and we observe layered stratified structures in $\delta\bar{\Sigma}_x$ and $\delta\bar{\rho}_x$.

3.3 Velocity distribution

The velocity field in normal unstratified turbulence is expected to follow a nearly Gaussian distribution, even for supersonic turbulence (fig. A1 in Federrath 2013), and the velocity magnitudes of different components are supposed to be isotropic. Here, we study the effect of stratification on the velocity distribution in different directions.

In Fig. 4, we show the PDFs of the different velocity components for two different Ri = 0.2 and Ri = 13. Clearly, all the individual component PDFs for both the simulations are nearly Gaussian. For Ri = 0.2, all the three component-PDFs nearly overlap with each other and have the same standard deviation. From now on, we use σ_{v_i} to denote the standard deviation of the velocity component along i. For Ri = 0.2, σ_{v_z} is only slightly lower than σ_{v_x} and σ_{v_y} whereas for Ri = 13, the standard deviation of velocity in different directions is clearly anisotropic, with $\sigma_{v_z} < \sigma_{v_x}, \sigma_{v_y}$.

This analysis shows that the velocity distribution is largely unaffected by the stratification if Ri $\lesssim 1$. However, for Ri $\gtrsim 1$, stratification strongly affects the velocity distribution by suppressing vertical motions. Also, strong gravity prevents turbulent mixing among different vertical layers (by flattening out the eddies along the direction of gravity), resulting in a small number of big two-dimensional eddies. This can lead to a difference between even σ_{v_x} and σ_{v_y} (see bottom panel in Fig. 3) due to low number statistics of these eddies.

3.4 PDF of density perturbations

For unstratified subsonic turbulence, the density is supposed to follow a lognormal distribution (Passot & Vázquez-Semadeni 1998; Federrath et al. 2008; Zhuravleva et al. 2013; Nolan, Federrath & Sutherland 2015) with some intermittency corrections (Hopkins 2013). Since our density distribution will be affected by stratification, we instead show the time-averaged volume-weighted distribution of s and fit the function $p_{\rm HK}(s)$ proposed by Hopkins (2013). It is defined as

$$p_{\rm HK}(s) = I_1\left(2\sqrt{\lambda w(s)}\right)\exp(-\lambda + w(s))\sqrt{\frac{\lambda}{\theta^2 w(s)}},$$

$$\lambda \equiv \sigma_{\rm s}^2/(2\theta^2),\ w(s) \equiv \lambda/(1+\theta) - s/\theta (w \geq 0), \qquad (15)$$

where $I_1(x)$ is the first-order modified Bessel function of the first kind. For further discussion on equation (15), refer to Hopkins (2013).

Fig. 5 shows these fits with the y-axis in log scale for different stratification runs. Clearly, density fluctuations are larger for stronger stratification, corroborating the trends seen in Figs 2 and 3. The density PDFs at lower levels of stratification (Ri $\lesssim 0.1$) show a low density tail, which is not well-accounted for by the fitting function.

The value of the intermittency parameter θ is small for all different levels of stratification – which implies that the distributions are close to lognormal. For $\theta = 0$, Hopkins' non-lognormal PDF $\approx$ lognormal PDF. There is a lot of variation in the lower and higher density tails. We have confirmed that this variability is not affected by limited numerical resolution (Fig. A1). For Ri $\gtrsim 1$, the PDFs

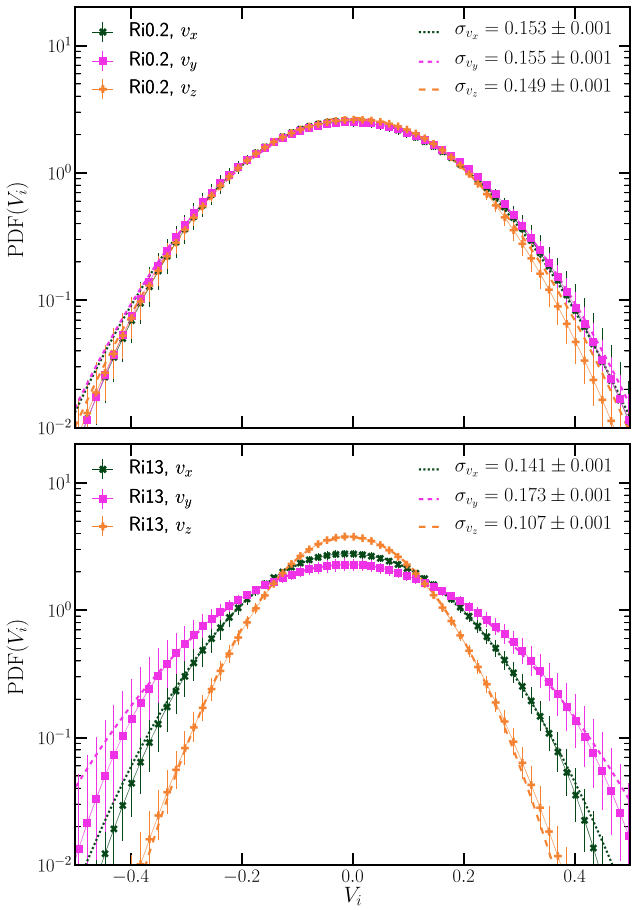

Figure 4. Time-averaged volume-weighted velocity-component PDFs with Gaussian fits for Ri = 0.2 *(top)* and Ri = 13 *(bottom)*. The PDFs are Gaussian for all three components, but the velocity fluctuation is anisotropic for Ri $\gtrsim 1$.

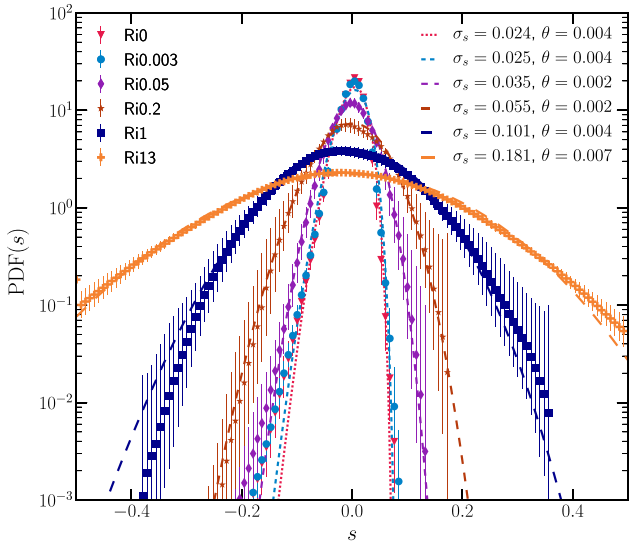

Figure 5. Volume-weighted PDF of s, fit using equation (15). The fluctuations (as characterized by the width of the PDF) are larger for stronger stratification. The intermittency parameter is close to 0, as is expected for subsonic turbulence.

do not show an asymmetric tail on the low-density side. This could be a result of density fluctuations being dominated by buoyancy oscillations instead of turbulent motions.

The low-density tail is known to be a feature of the density PDFs when the adiabatic index $\gamma > 1$. Hopkins (2013)' fit was shown to be a good fit for density PDF of gas following an isothermal equation of state, which has $\gamma = 1$. We expect γ to be a parameter of the distribution function (Nolan et al. 2015).

3.5 Density fluctuation σ_s as a function of Ri

Here, we study the effect of stratification, parametrized by Ri, on the density fluctuation–Mach number (σ_s–Ri) relation, and try to derive a theoretical scaling relation between the two. Other than its theoretical importance, these relations can be useful for estimating the velocity fluctuations from X-ray brightness observations of clusters. Once the rms density fluctuations are known from SB maps, the velocity fluctuation can be calculated using these relations or similar relations between their spectra (Zhuravleva et al. 2013, 2014b).

For our simulations with Ri $\gtrsim 1$, the local Ri changes with z. Thus, we first create bins uniform in $\log_{10}$(Ri). If for a particular simulation, the Ri value range falls in two different consecutive bin-ranges, we split the data at $z = z_0$, where $\mathrm{Ri}(z_0) = \mathrm{Ri}_{\text{bin boundary}}$ between the two bins. These two data sets are cuboids with $-L/2 \leq z < z_0$ and $z_0 \leq z \leq L/2$. We then calculate σ_s for these data sets separately. This method takes the variation of Ri as a function of z within the simulation domain into account.

The upper panel of Fig. 6 shows σ_s as a function of Ri. We see that σ_s increases with Ri for Ri $\gtrsim 0.01$ and the increase seems to slow down around Ri $\gtrsim 1$. In the remaining part of this subsection, we attempt to derive a fitting function for this relation. We focus on the weakly stratified turbulence regime, with $0.01 \lesssim \mathrm{Ri} \lesssim 1$. The net density perturbations can be written as a sum of fluctuations due to unstratified turbulence and stratification, given by

$$\delta\bar{\rho}^2 = \delta\bar{\rho}^2_{\text{buoyancy}} + \delta\bar{\rho}^2_{\text{turb}}. \tag{16}$$

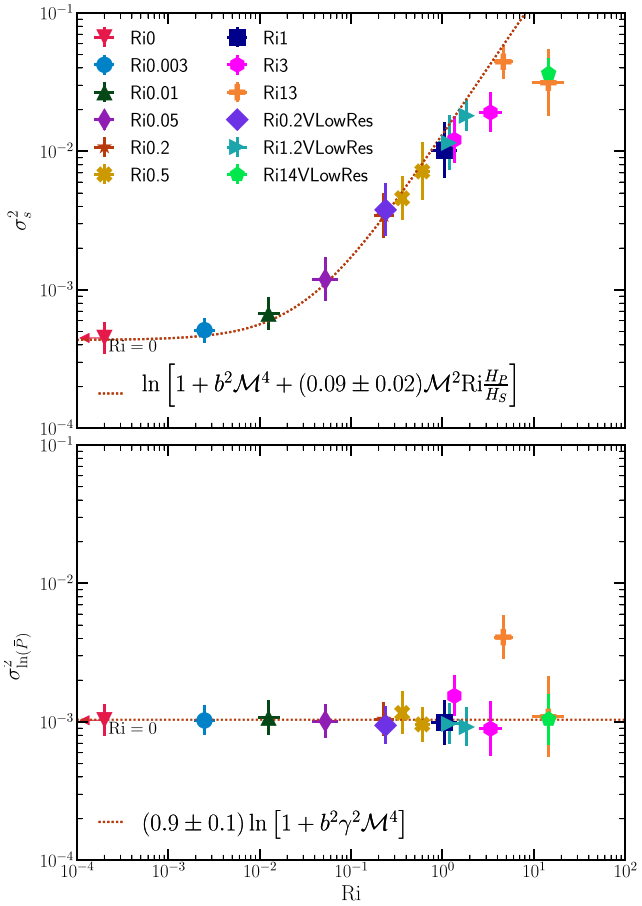

Figure 6. *Upper panel:* Scatter plot of σ_s versus Ri. The amplitude of density fluctuations increases as a function of Ri for $0.01 \lesssim \mathrm{Ri} < 1$, reaches a peak at Ri ≈ 10 and then starts decreasing for Ri > 10. *Lower panel*: Scatter plot of $\sigma_{\ln(\bar{P})}$ (defined in Section 3.6) versus Ri. Pressure fluctuations are roughly independent of Ri. The outlier point has a larger local $\mathcal{M}$ which makes it consistent with the baseline relation. *Note:* We conduct 'VLowRes' runs with resolution $256^2 \times 384$, but with different H_P/H_ρ (and thus different H_P/H_S), with simulation parameters described in Table 2. For these runs, we have plotted $\sigma_{s,\,\text{scaled}}$ calculated using equation (21) instead of σ_s.

In Mohapatra & Sharma (2019), we showed that $\delta\bar{\rho}^2_{\text{turb}} \propto \mathcal{M}^4$. Here, we attempt to derive an expression for $\delta\bar{\rho}^2_{\text{buoyancy}}$. Substituting N^2 from equation (6d) in equation (6c), we obtain

$$\left\langle \delta\bar{\rho}^2_{\text{buoyancy}} \right\rangle = \frac{N^4}{g^2}\left\langle \delta z^2 \right\rangle. \tag{17}$$

We assume that the rms displacement of a parcel of gas in the turbulence dominated regime (Ri < 1) is proportional to the driving length-scale. Thus, we substitute $\left\langle \delta z^2 \right\rangle = \zeta^2 L^2_{\text{driv}}$, where L_{driv} is the turbulence driving length-scale and ζ is a dimensionless constant. $N^2 = \frac{g}{\gamma}\frac{\mathrm{d}S}{\mathrm{d}z} = \frac{g}{\gamma H_S}$. This gives us

$$\left\langle \delta\bar{\rho}^2_{\text{buoyancy}} \right\rangle = \frac{\zeta^2 L^2_{\text{driv}}}{\gamma^2 H_S^2} \tag{18a}$$

$$= \frac{\zeta^2 \mathrm{Ri}\mathcal{M}^2 c_s^2}{N^2\gamma^2 H_S^2} \text{ (using equation 8)} \tag{18b}$$

$$= \zeta^2\mathcal{M}^2\mathrm{Ri}\frac{H_P}{H_S} \text{ (substituting } N \text{ from equation 6}d\text{)}. \tag{18c}$$

Table 2. Simulation parameters for very low resolution runs.

Label (1)	Ri (2)	H_ρ (3)	H_P (4)	σ_s (5)	$\sigma_{\mathrm{s,\,scaled}}$ (6)
Ri0.2VLowRes	0.2 ± 0.1	1.5	1.25	0.03 ± 0.01	0.06 ± 0.03
Ri1.2VLowRes	1.2 ± 0.4	0.75	0.75	0.06 ± 0.03	0.11 ± 0.06
Ri14VLowRes	14^{-8}_{+20}	0.25	0.25	0.11 ± 0.03	0.20 ± 0.05

Note. All these simulations have grid resolution $256^2 \times 384$ and $\mathcal{M} \approx 0.25$. The columns (2)–(5) have their usual meanings. For these runs, $H_\mathrm{P}/H_\rho \neq 2$, unlike our runs in Table 1. In column 6, we show $\sigma_{\mathrm{s,\,scaled}}$, which we calculate using equation (21).

Inspired by the density fluctuation–Mach number relations in Nolan et al. (2015) and Mohapatra & Sharma (2019), we combine the two rms values of density perturbations and propose a new relation

$$\sigma_\mathrm{s}^2 = \ln\left(1 + b^2\mathcal{M}^4 + \zeta^2\mathcal{M}^2\mathrm{Ri}\frac{H_\mathrm{P}}{H_\mathrm{S}}\right), \tag{19}$$

where b stands for the turbulence driving parameter and $b = 1/3$ for solenoidal forcing (Federrath et al. 2008, 2010). We use ζ^2 in equation (19) as a fitting parameter for Fig. 6 and obtain $\zeta^2 = 0.09 \pm 0.02$.

For $\mathrm{Ri} = 0$ (unstratified turbulence), this reduces to $\sigma_\mathrm{s}^2 = \ln(1 + b^2\mathcal{M}^4)$, which reproduces the $\sigma_{\bar{\rho}} \propto \mathcal{M}^2$ scaling relation in Mohapatra & Sharma (2019). This relation for unstratified turbulence was motivated for subsonic flows by assuming the flow to be close to incompressible. In such a case, taking the divergence of equation (1b) gives the Poisson equation $\nabla^2 P = \nabla \cdot (\nabla \cdot (\rho \mathbf{v} \otimes \mathbf{v})) = \rho(\nabla\mathbf{v})^\mathrm{T} : \nabla\mathbf{v}$, which on simplifying gives $\delta P \sim \rho\delta v^2$, or $\delta\bar{P} \sim \gamma\delta v^2/c_\mathrm{s}^2 \sim \gamma\mathcal{M}^2$. Now since these fluctuations are adiabatic (Mohapatra & Sharma 2019), $\delta\bar{\rho} = \delta\bar{P}/\gamma \propto \mathcal{M}^2$. Comparing this relation to the gamma-dependent σ_s–$\mathcal{M}$ relation of Nolan et al. (2015) for $\gamma = 5/3$, who obtain $\sigma_\mathrm{s}^2 = \ln(1 + b^2\mathcal{M}^{28/9}) \approx \ln(1 + b^2\mathcal{M}^{3.1})$, which is shallower compared to our proposed relation. This discrepancy arises because our simulations are subsonic while their fits are obtained for the transonic regime. A flattening of σ_s versus $\mathcal{M}$ for $\mathcal{M} \sim 1$ is also seen in fig. 1 of Mohapatra & Sharma (2019).

Taking the ratio of the two types of density fluctuations, we obtain

$$\frac{\delta\bar{\rho}^2_\mathrm{buoyancy}}{\delta\bar{\rho}^2_\mathrm{turb}} = \frac{0.09\mathrm{Ri}}{b^2M^2}\frac{H_\mathrm{P}}{H_\mathrm{S}} \approx 30\,\mathrm{Ri}, \tag{20}$$

inserting all other parameters which are constant for our simulations. Thus the effects of stratification should start dominating for $\mathrm{Ri} \gtrsim 0.03$, which is exactly what we see in our simulations.

For $\mathrm{Ri} \gtrsim 1$, the eddies start becoming flatter in the z-direction (see Fig. 3, fourth row panels), so ζ should depend on Ri. We expect ζ to decrease with increasing Ri but we have not obtained a functional form for its dependence. Also for simulations with $\mathrm{Ri} \gtrsim 1$, both Ri and $\mathcal{M}$ show large variations within the simulation domain as a function of z. Obtaining an accurate and reliable σ_s–$\mathcal{M}$–Ri relation for $\mathrm{Ri} \gtrsim 1$ is beyond the scope of this study.

In order to check the dependence of σ_s on $H_\mathrm{P}/H_\mathrm{S}$, we have run three simulations with grid resolution $256^2 \times 384$ and different values of this parameter (Table 2). We use a constant value of $H_\mathrm{P}/H_\mathrm{S}$ (corresponding to $H_\mathrm{P}/H_\rho = 2$) in fitting σ_s–$\mathcal{M}$–Ri relation shown in the upper panel of Fig. 6. To compare with our fit based on high-resolution runs with $H_\mathrm{P}/H_\rho = 2$, we scale σ_s values from these simulations to $\sigma_{\mathrm{s,\,scaled}}$, which accounts for a different $H_\mathrm{P}/H_\mathrm{S}$ in equation (19). The scaled σ_s is given by

$$\sigma_{\mathrm{s,scaled}} = \ln\left[1 + b^2\mathcal{M}^4 + f_\mathrm{scale}\left(\exp(\sigma_\mathrm{s}) - \left(1 + b^2\mathcal{M}^4\right)\right)\right],$$

$$\text{where } f_\mathrm{scale} = \frac{H_\mathrm{P}/H_\mathrm{S}|_{H_\mathrm{P}/H_\rho=2}}{H_\mathrm{P}/H_\mathrm{S}|_{H_\mathrm{P}/H_\rho}}. \tag{21}$$

This scaling is equivalent to multiplying $\delta\bar{\rho}^2_\mathrm{buoyancy}$ with f_scale (see equation 18c).

Shi & Zhang (2019) study the decay of a turbulent velocity field in a stratified medium and find that normalized density dispersion $\sigma_{\bar{\rho}}$ is smaller than the saturated value initially, stays roughly constant, and saturates after $t \gtrsim 1/N$ to $\sigma_{\bar{\rho}} = 0.59\mathcal{M}$ as turbulence decays with time and $\mathcal{M}$ decreases (see their figure 8). Their temporal behaviour is consistent with our σ_s–$\mathcal{M}$–Ri relation, since the density fluctuations due to buoyancy with moderate stratification only depend on the driving scale and the entropy scale height (Equation 18a). These are held fixed while $\mathcal{M}$ decreases and Ri increases with time in decaying turbulence. At late times $\mathrm{Ri} \gtrsim 10$, σ_s decreases linearly with decreasing $\mathcal{M}$ (fig. 8 in Shi & Zhang 2019) as we enter the strongly stratified regime, and vertical displacement and σ_s are suppressed. This regime will be investigated further in a follow-up study.

Equation (18a) shows that the net density perturbations depend only on the driving length-scale of turbulence and not on the velocity itself – this would have significant implications for obtaining velocity from SB fluctuations. We also find that σ_s depends on three dimensionless parameters instead of just one – $\mathcal{M}$, Ri, and the ratio between the entropy and pressure scale heights, $H_\mathrm{S}/H_\mathrm{P}$. Thus, one cannot have a universal relation between density and velocity fluctuations.

3.6 Pressure fluctuation $\sigma_{\ln(\bar{P})}$ as a function of Ri

We now shift our focus to the relation between pressure fluctuations and Mach number, and its dependence on stratification. Pressure fluctuations can be inferred from the SZ observations of clusters – using this relation, we can estimate turbulent velocities on cluster outskirt scales ($\gtrsim$500 kpc) (Khatri & Gaspari 2016; Mroczkowski et al. 2019; Simionescu et al. 2019). A measurement of the turbulent velocity dispersion is required to calculate the level of non-thermal pressure support and thus the hydrostatic mass bias in clusters (Cavaliere et al. 2011; Nelson et al. 2014).

In the lower panel of Fig. 6, we show $\sigma_{\ln(\bar{P})}$ as a function of Ri. Here, $\sigma_{\ln(\bar{P})}$ is the standard deviation of $\ln(\bar{P})$ distribution and is analogous to σ_s for density. We find that $\sigma_{\ln(\bar{P})}$ is almost independent of the stratification. Among the two kinds of density fluctuations, $\delta\bar{\rho}_\mathrm{buoyancy}$ is isobaric so $\delta\bar{P}_\mathrm{buoyancy} = 0$, whereas $\delta\bar{\rho}_\mathrm{turb}$ is adiabatic, so $\delta\bar{P}_\mathrm{turb} = \gamma\delta\bar{\rho}_\mathrm{turb}$. Thus, the expression for the relation becomes

$$\sigma_{\ln(\bar{P})} = \ln(1 + b^2\gamma^2\mathcal{M}^4), \tag{22}$$

which is independent of Ri. For $\mathrm{Ri} \gtrsim 1$, we see some variations in $\sigma_{\ln(\bar{P})}$. Since these simulations have large temperature gradients within the simulation domain (check Table 1 for H_P and H_ρ), the Mach number can vary as a function of z even if we drive a homogeneous isotropic velocity field. This may cause $\sigma_{\ln(\bar{P})}$ to overshoot or undershoot.

While the σ_s–$\mathcal{M}$ fluctuation relation also depends on other parameters such as $H_\mathrm{P}/H_\mathrm{S}$ and Ri, the $\sigma_{\ln(P)}$–$\mathcal{M}$ relation is independent of the stratification strength and the pressure and entropy scale heights. In Mohapatra & Sharma (2019), we showed that the $\sigma_{\bar{P}}$–$\mathcal{M}$ relation depended on the thermodynamics (heating and cooling) whereas the $\sigma_{\bar{\rho}}$–$\mathcal{M}$ relation was independent of the

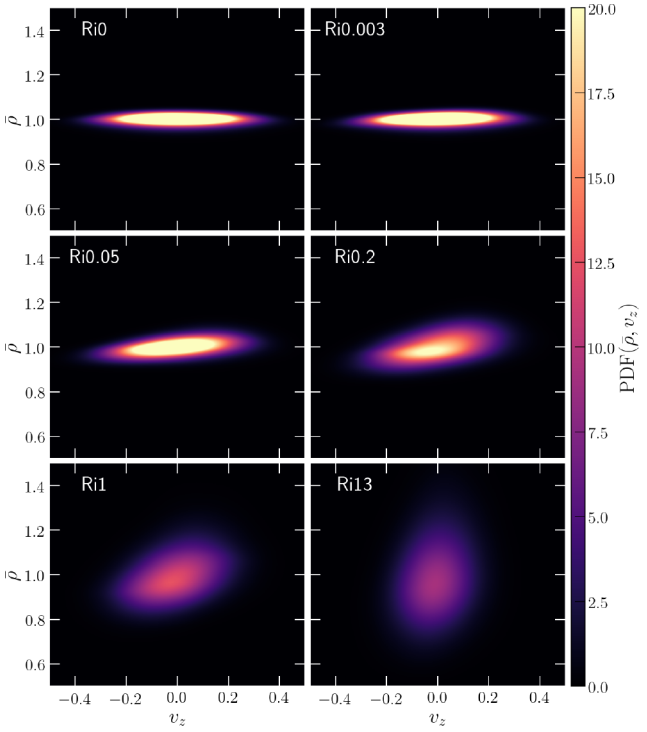

Figure 7. Volume-weighted 2D PDF of $\bar{\rho}$ versus v_z. As the strength of the stratification increases (10^{-3} < Ri < 1) at constant $\mathcal{M} = 0.25$, the PDF tilts anticlockwise showing a local correlation between density and v_z. The correlation weakens for Ri $\gtrsim 1$.

thermodynamics, and still followed the same relation as homogeneous isotropic turbulence. Thus, for subsonic turbulence ($\mathcal{M} < 1$), pressure fluctuations are independent of the thermodynamics and the stratification strength – so they appear more reliable for estimating the velocity dispersion. This has important implications for different methods of measuring velocities and estimating the non-thermal pressure component in cluster outskirts. Higher resolution SZ observation of clusters in future can also help us get velocities on smaller scales – which are more relevant for understanding CCs.

3.7 Correlation between v_z and density perturbations

In the run Ri0.2, one can observe a correlation between the signs of v_z and the column density perturbations (second row from top, second, and third columns, Fig. 3). The red regions ($\delta\bar{\Sigma}_x > 0$ and $\delta\bar{\rho}_x > 0$) are more populated with upward facing arrows ($v_z > 0$) and the blue regions ($\delta\bar{\Sigma}_x < 0$ and $\delta\bar{\rho}_x < 0$) are more populated with downward facing arrows ($v_z < 0$). To look more into this, in Fig. 7 we show two-dimensional volume-weighted probability distribution functions (2D PDFs) of normalized density fluctuations ($\delta\bar{\rho}$) and v_z. For unstratified turbulence (Ri = 0), $\bar{\rho}$ and v_z are not locally correlated since turbulence is homogeneous and isotropic. As the stratification strength increases, the PDF starts rotating anticlockwise, showing a positive correlation between the direction of v_z and the sign of $\delta\bar{\rho}$. However, for the strongest stratification runs, this correlation disappears. The spread in v_z becomes narrower with increasing Ri and the spread in $\bar{\rho}$ increases.

A positive correlation between density fluctuations and vertical velocities is a consequence of the work done against the buoyancy force which converts kinetic energy into potential energy. It is a hallmark of stably stratified turbulence (Verma 2018). For very strong stratification with Ri > 10, the $\delta\bar{\rho}$–v_z correlation disappears, since now BV oscillations are generated by turbulent motions. This second transition is seen in the last two panels of Fig. 7. Further, turbulent motions along the z-direction are heavily suppressed due to strong stratification. When we catch a parcel of gas with $\delta z > 0$ and $\delta\rho > 0$, we are equally likely to catch it in the rising and falling parts of its oscillatory motion and $v_{z,\,\mathrm{BV}}$ and δz are not correlated. This is reminiscent of the phase plot (a plot of position versus velocity) of a simple harmonic oscillator.

3.8 Nature of density perturbations

X-ray observations of clusters have been used to characterise brightness fluctuations (caused by density fluctuations) according to their equation of state (Arévalo et al. 2016; Churazov et al. 2016; Zhuravleva et al. 2018). By comparing the emission in hard and soft X-ray bands, Zhuravleva et al. were able to categorise these fluctuations into adiabatic, isobaric or isothermal density fluctuations.

We aim to distinguish between the two kinds of density perturbations in our simulations – the first caused by unstratified turbulence ($\delta\rho_{\mathrm{turb}}$) and the second introduced due to buoyancy and stratification ($\delta\rho_{\mathrm{buoyancy}}$). We can do so by differentiating between the nature (the effective equation of state or EOS) of these perturbations. Without stratification, $\delta\rho = \delta\rho_{\mathrm{turb}}$. In this case, we expect density fluctuations due to subsonic turbulence to be adiabatic ($\delta P/P = \gamma\delta\rho/\rho$) (Mohapatra & Sharma 2019). This is simply a consequence of a fluid element conserving its entropy over a time shorter than the turbulent turnover time.

As we increase Ri, we expect the contribution of $\delta\rho_{\mathrm{buoyancy}}$ to increase. To understand the nature of these buoyant density fluctuations, consider the parcel from Section 2.3 again. When this parcel of gas rises, it is in constant pressure equilibrium with its surroundings (as its motion is subsonic). So $\delta P = 0$ for the parcel in its new environment. The movement of the parcel only causes an overall change in its density with respect to its immediate surroundings. Hence, density fluctuations caused by buoyancy should be effectively isobaric in nature for subsonic velocities ($\mathcal{M} < 1$).

To confirm our two hypotheses, we show 2D PDFs of $\bar{P}$ and $\bar{\rho}$ and look for possible correlations between them (Fig. 8). The two dashed lines indicate the relations between density and pressure if the fluctuations were adiabatic ($\delta\bar{P} = \gamma\delta\bar{\rho}$) and isobaric ($\delta\bar{P} = 0$), respectively. The total density fluctuations can be given by equation (16). As expected, the PDF for unstratified turbulence closely follows the adiabatic EOS fit with little spread. Further on increasing stratification, the PDF starts spreading out horizontally due to the increasing contribution of isobaric density fluctuations. This is because the contribution of $\delta\rho_{\mathrm{buoyancy}}$ to $\delta\rho$ increases, in agreement with what we expected.

Zhuravleva et al. (2018) find that for most clusters, the density fluctuations in the inner half of cool-cores are either isothermal or isobaric. We propose that density fluctuations caused by turbulent motion of gas in a stratified medium can be a key contributor to the isobaric density fluctuations. Thermal conduction can make density fluctuations isothermal at small scales, but a detailed investigation of this is beyond the scope of this study.

3.9 Power spectra

While all the 1D and 2D PDFs tell us about different global statistics of stratified turbulence, we are also interested in the

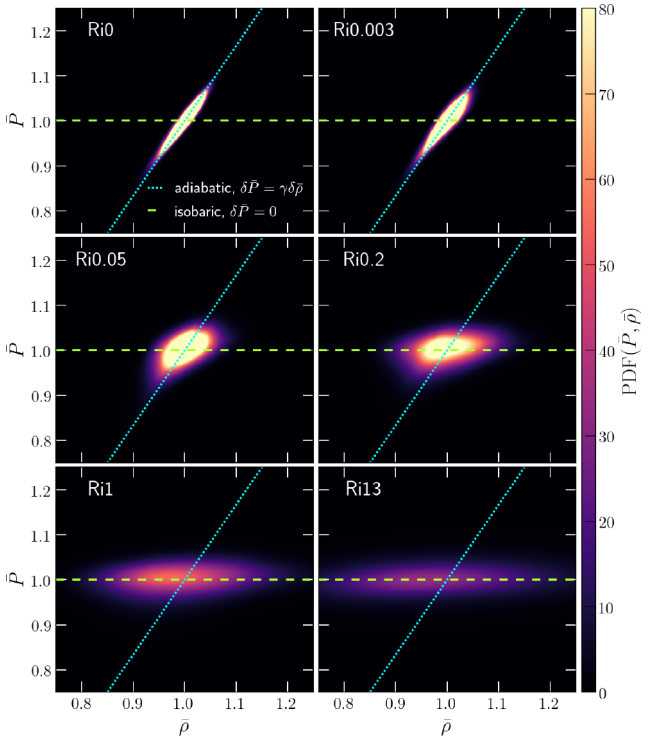

Figure 8. Volume-weighted 2D PDF of $\bar{P}$ versus $\bar{\rho}$ for different stratification runs (10^{-3} < Ri < 1, constant $\mathcal{M} = 0.25$), with fits showing the nature of the perturbations. For the adiabatic fit, $\delta P/ < P > = \gamma \delta\rho/ < \rho >$, and for the isobaric fit, $\delta P/ < P > = 0$. Fluctuations are isobaric for strong stratification and become increasingly adiabatic with the decreasing strength of the stratification.

spatial scaling of density and velocity perturbation fields. One way to study the scale dependence is by computing power spectra of these fields. Recent observational works such as Zhuravleva et al. (2014a, 2018) have used power spectra to calculate density and velocity fluctuations of ICM gas as a function of scale. Theoretical studies such as Zhuravleva et al. (2013) and Gaspari et al. (2014) model these relations between density and velocity power spectra in cosmological simulations and large-scale cluster simulations, respectively. However, in Fig. 1 we showed that Ri can vary significantly with radial distance from the cluster centre. Hence, we need to study the power spectra on local scales, so that we can study the dependency (if any) of these power spectra on Ri. Then we can use these models to relate density and velocity spectra based on Ri as a function of radius in the ICM.

By following different binning methods in k-space, we can also study the effect of stratification-induced anisotropy on the distribution of power in different directions (perpendicular and parallel to the stratification direction).

3.9.1 Velocity power spectra

We show the power spectrum of the local Mach number (velocity in units of the local sound speed) $P(\mathcal{M}_k)$ in the top panel of Fig. 9. To evaluate these spectra, we bin power in Fourier space in spherical shells of width $\delta k = 1$ centred at $\mathbf{k} = 0$. We compensate $P(\mathcal{M}_k)$ by the Kolmogorov (1941) scaling ($k^{-5/3}$) of velocities for homogeneous isotropic incompressible turbulence. $P(\mathcal{M}_k)$ neither changes in slope nor in amplitude with changing strengths of stratification. The constant amplitude is expected

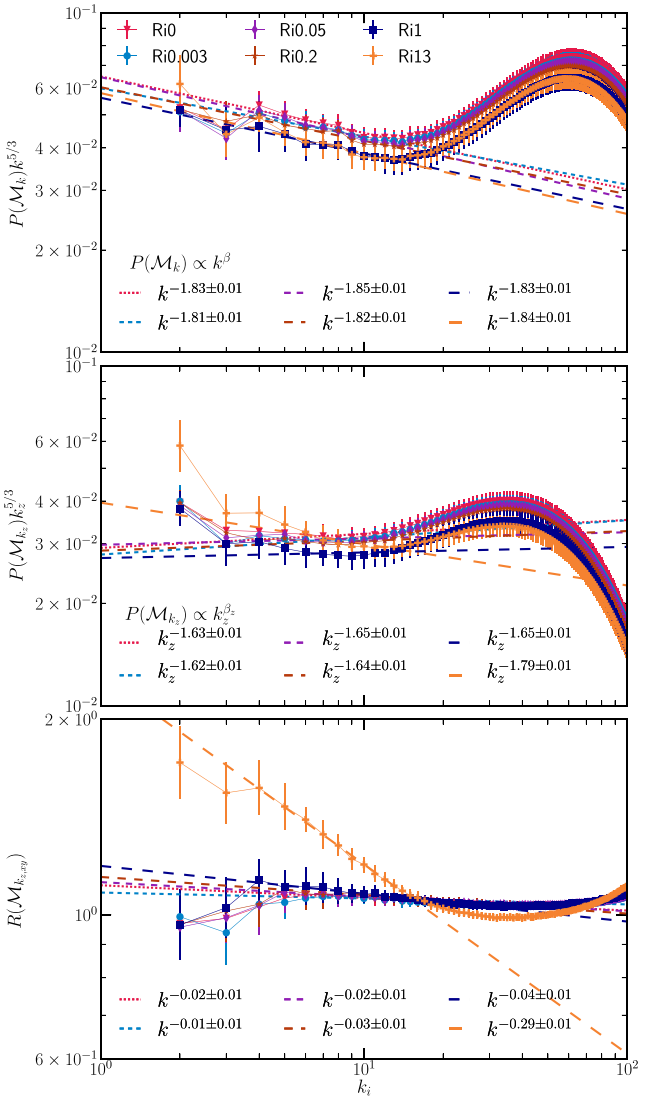

Figure 9. *Upper panel:* Time-averaged compensated power spectra of Mach number (velocity fluctuations normalized to the sound speed) for our standard set of runs with Ri indicated in labels. The slope of the power spectrum in the inertial range is steeper than the Kolmogorov scaling, but does not vary much with Ri. *Middle panel*: The same as the top panel, but with binning along k_z. *Lower panel:* Ratio of Mach number power spectra in vertical (z) and horizontal (x, y) modes, $R(\mathcal{M}_{k_{z,xy}}) = P(\mathcal{M}_{k_z})/(0.5(P(\mathcal{M}_{k_x}) + P(\mathcal{M}_{k_y}))$. *Note:* All fit slopes indicated in legends are fits for the corresponding power spectra and not for compensated power spectra.

since $\mathcal{M} \approx 0.25$ for all runs. We find slopes of $P(\mathcal{M}_k)$ in the range -1.81 ± 0.01 to -1.86 ± 0.01, without any obvious systematic dependence on Ri. The spectrum is steeper than the Kolmogorov scaling as is expected from intermittency effects (She & Leveque 1994; Boldyrev, Nordlund & Padoan 2002; Schmidt, Federrath & Klessen 2008; Konstandin et al. 2012; Federrath 2013). She & Leveque (1994) predict a steepening of the power spectrum by ≈0.03 for incompressible turbulence. However, here we are dealing with mildly compressible turbulence ($\mathcal{M} \sim 0.25$), which leads to additional steepening of the velocity power spectrum (Aluie 2011; Galtier & Banerjee 2011; Banerjee & Galtier 2013, 2014; Federrath 2013).

In order to understand the trends in the spectra and to look at the distribution of power perpendicular and parallel to the stratification direction, we bin the squared Fourier amplitudes separately along slabs of constant k_i, with $\delta k_i = 1$, centred at $k_i = 0$, where i can be x, y, or z. We denote these as $P(\mathcal{M}_{k_i})$. We also compute the ratio of power parallel and perpendicular to the stratification direction, denoted by $R(\mathcal{M}_{k_{z,xy}})$, where $R(\mathcal{M}_{k_{z,xy}}) = P(\mathcal{M}_{k_z})/(0.5(P(\mathcal{M}_{k_x}) + P(\mathcal{M}_{k_y}))$. We show $P(\mathcal{M}_{k_z})$ in the middle panel of Fig. 9, compensated by $k_z^{-5/3}$. In the lower panel, we show $R(\mathcal{M}_{k_{z,xy}})$. One can infer the scaling perpendicular to k_z and the amplitude of velocity fluctuations by dividing the slopes of the middle panel by those in the lower panel.

From the middle panel of Fig. 9, we observe that while the amplitude of the power spectrum remains almost the same, the slope of $P(\mathcal{M}_{k_z})$ steepens around Ri $\gtrsim 1$. This is due to anisotropy effects – the eddies in strongly stratified turbulence are flattened (like pancakes) parallel to the direction of gravity (see lower panel of Fig. 3). Thus, $k_z \gg k_x$, k_y, and the power spectrum $P(\mathcal{M}_{k_z})$ becomes steeper with increasing Ri for Ri > 1. It can be clearly seen in the lower panel of Fig. 9, where $R(\mathcal{M}_{k_{z,xy}})$ is almost flat for Ri < 1 and steepens significantly for Ri $\gtrsim 1$, $k \lesssim 20$.

3.9.2 *Density power spectra*

Now, we study the effect of stratification and anisotropy on the amplitude of density perturbations over different scales. We do so by computing the power spectrum of $\bar{\rho}$ (compensated by $k^{-5/3}$ Corrsin 1951 scaling of passive scalars), in the top panel of Fig. 10 for different runs. As expected, the amplitude of the power spectrum increases with increasing stratification, by almost two orders of magnitude, as quantified in detail in Section 3.5. The density power spectrum for unstratified turbulence overlaps with the weakly stratified run with Ri $= 0.003$.

As for the velocity power spectra, we study the effects of anisotropy by computing $P(\bar{\rho}_{k_i})$, where $i = x$, y, or z, binned similar to $P(\mathcal{M}_{k_i})$ along k_i. We also compute the ratio of power parallel and perpendicular to the stratification direction, denoted by $R(\bar{\rho}_{k_{z,xy}}) = P(\bar{\rho}_{k_z})/(0.5(P(\bar{\rho}_{k_x})) + P(\bar{\rho}_{k_y}))$. We show $P(\bar{\rho}_{k_z})$ in the middle panel of Fig. 10, compensated by $k_z^{5/3}$. In the lower panel, we show $R(\bar{\rho}_{k_{z,xy}})$. For $P(\bar{\rho}_{k_z})$, we see the same trend as for $P(\bar{\rho}_k)$, in the sense that it increases in amplitude and the power spectrum first becomes shallower with increasing Ri and then starts becoming steeper again for Ri $\gtrsim 1$. For $R(\bar{\rho}_{k_{z,xy}})$, the slope remains close to zero for Ri < 1 and becomes steeper for Ri $\gtrsim 1$, which is very similar to what we observed for $R(\mathcal{M}_{k_{z,xy}})$.

We show α, the spectral index of $P(\bar{\rho}_k)$ in Fig. 11. For low Ri $\lesssim 0.01$, α is more negative than the theoretically predicted Corrsin (1951) scaling ($k^{-5/3}$). With increasing stratification, the value of α initially starts to rise, peaks at Ri ~ 1 and then falls again for Ri > 1.

The above trends reflect the two transitions we observe as we increase Ri from ≈0.001 to ≈13. The first transition occurs around $0.001 <$ Ri < 0.01, when $\delta\rho_{\rm buoyancy}$ starts dominating over $\delta\rho_{\rm turb}$. As seen in the power spectrum, unstratified turbulence by itself is unable to drive small-scale density perturbations very efficiently, due to which $P(\bar{\rho}_k)$ is much steeper than the velocity power spectrum. However, with weak stratification, when the velocity distribution is still quite isotropic, $\delta\bar{\rho}$ is locally correlated to v_z, and the slope of the power spectrum becomes shallower and closer to the slope of the velocity power spectrum. On increasing stratification beyond Ri > 1, the eddies become more pancake-like in shape.

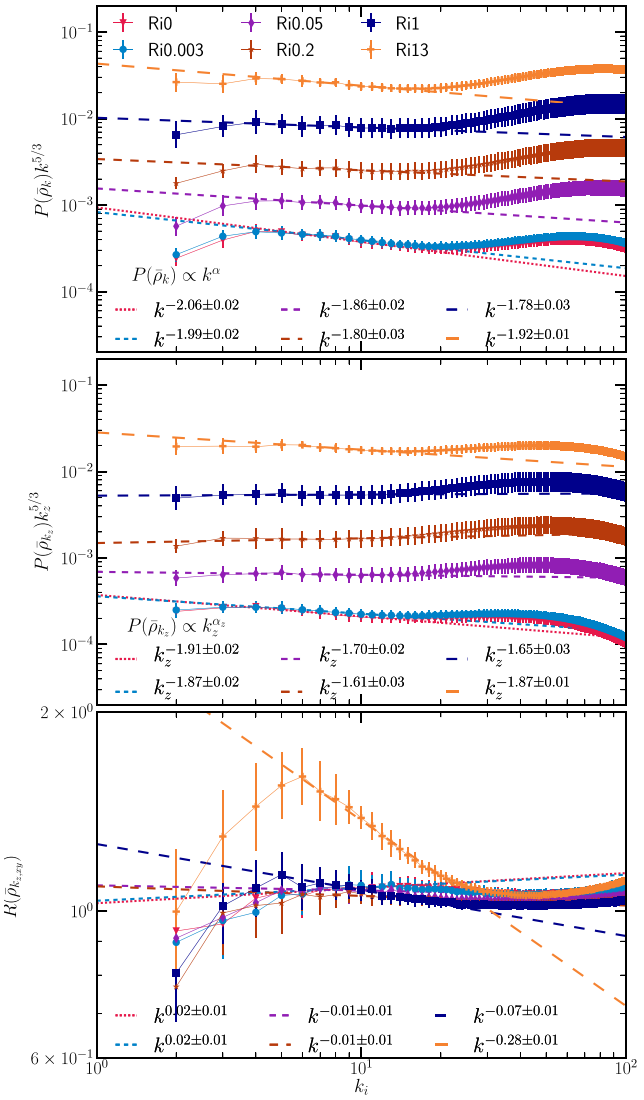

Figure 10. *Upper panel:* Time-averaged compensated power spectra of density fluctuations for different runs with Ri indicated in the run labels. The slope of the power spectrum in the inertial range decreases as a function of Ri. It becomes closer to Corrsin (1951) scaling at large Ri. *Middle panel*: The same as the top panel, but with binning along k_z. *Lower panel:* Ratio of normalized density power spectra in vertical (z) and horizontal (x, y) modes, $R(\bar{\rho}_{k_{z,xy}}) = P(\bar{\rho}_{k_z})/(0.5(P(\bar{\rho}_{k_x}) + P(\bar{\rho}_{k_y}))$. *Note:* All fit slopes indicated in legends are fits for the corresponding power spectra and not for compensated power spectra.

This leads to a decrease in v_z, and $k_z > k_x$, k_y. Since the vertical motions of gas are still the dominant contributor to the total density fluctuations ($\delta\rho_{\rm buoyancy} > \delta\rho_{\rm turb}$ for Ri > 0.03), the overall power spectrum also becomes steeper.

One can calculate the slopes of the perpendicular density power spectrum ($P(\bar{\rho}_{k_{xy}}) = 0.5(P(\bar{\rho}_{k_x}) + P(\bar{\rho}_{k_y}))$ by dividing the slope of the middle panel by the corresponding slopes of the lower panel. The slope of $P(\bar{\rho}_{k_{xy}})$ only becomes shallower till Ri ≈ 1 and then saturates at that value. This shows that strong stratification affects density modes only in the direction parallel to the stratification.

Gaspari & Churazov (2013) also derive the relation between gas density and velocity power spectra in their simulations. They find that normalized density fluctuations vary with the Mach number as $\delta\bar{\rho} \simeq 1/4\mathcal{M}$. However, they use a fixed stratification profile for

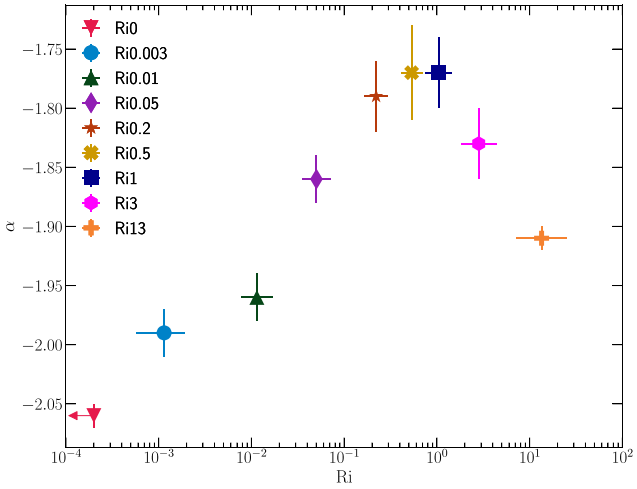

Figure 11. Scatter plot of α, the slope of density power spectrum ($P(\bar{\rho}_k) \propto k^{\alpha}$). The slope becomes shallower with increasing Ri and peaks at Ri $\sim$ 1 (Fig. 9) before steepening again for Ri $>$ 1.

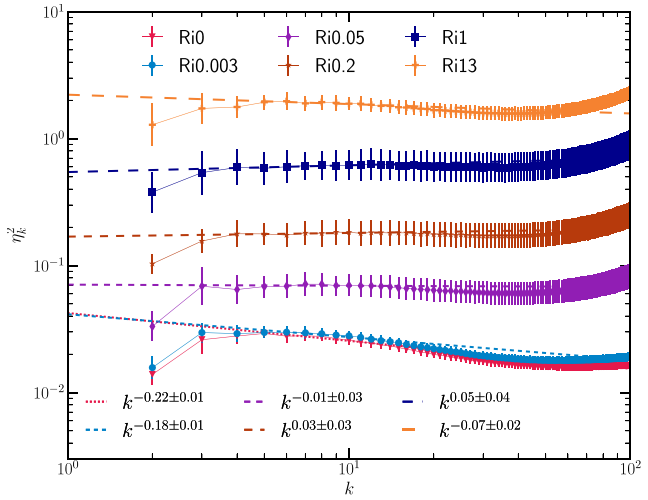

Figure 12. Ratio of density and velocity power spectra, η_k^2, for our standard set of runs. We see that η_k increases with increasing Ri.

all their simulations. Their relation is very likely a result of strong stratification with Ri $\gtrsim$ 10. Fig. 1 shows the variation in Ri as a function of radius and equation (19) is our density fluctuation–Mach number relation. Clearly, different terms in our relation will dominate in parts of the cluster.

3.9.3 Ratio between density and velocity power spectra

Zhuravleva et al. (2014b) derive the relation between density and 1D velocity Fourier amplitudes $\delta\rho_k$ and $v_{1,k}$, respectively. They show that the ratio of the normalized power spectra, given by[2]

$$\eta_k = (\delta\rho_k/\langle\rho\rangle)/(v_{1,k}/c_s) \approx \sqrt{3P(\bar{\rho}_k)/P(\mathcal{M}_k)}, \quad (23)$$

is nearly constant with $\eta_k \approx 1.0 \pm 0.3$ and independent of length-scale or $\mathcal{M}$.

We show η_k^2 in Fig. 12 and find that it increases with the stratification strength, with $0.01 \lesssim \eta_k^2 \lesssim 1$ for our simulations, and its amplitude increases with increasing Ri. The ratio η_k is roughly independent of k only for $0.05 \lesssim$ Ri $\lesssim 2$, when the density and velocity power spectra are parallel due to the correlation we discussed in Section 3.7. Thus, most importantly, the conversion of density perturbations into velocity perturbations is not universal.

Our conclusion that η_k^2 increases with Ri can be reconciled with previous works that find it to be universal, because the latter are in the strongly stratified (Ri $\gtrsim$ 10) limit. The clusters in Zhuravleva et al. (2014b) indeed have an estimated Ri $\gtrsim$ 10 (Zhuravleva, private communication), which makes our results consistent. This interpretation is also in agreement with the stratified decaying simulations of Shi & Zhang (2019), who find a saturation of η_k^2 as the atmosphere becomes strongly stratified (see their fig. 8). A saturation of η_k^2 for Ri $\gtrsim$ 10 implies that the rms density fluctuations will also saturate at a small amplitude ($[\delta\rho/\rho]_{\rm rms} \lesssim$ 0.2; our preliminary simulations for Ri $>$ 10 agree with this). Small amplitude density fluctuations mean that multiphase condensation in the ICM occurs in the low perturbation amplitude limit (see figs 6 and 11 of Choudhury, Sharma & Quataert 2019). Large density perturbations that produce multiphase gas more easily can only be induced in the wakes of dense structures such as galaxies and intergalactic filaments.

4 COMPARISONS, CAVEATS, AND FUTURE WORK

Kumar et al. (2014) study the passive scalar power spectrum in stratified turbulence. Several other studies (e.g. Carnevale, Briscolini & Orlandi 2001; Lindborg 2006; Deusebio, Vallgren & Lindborg 2013) discuss the transition between buoyancy and inertial length-scale in the power spectra of velocity and passive scalars at the Bolgiano length-scale l_B. In Bolgiano–Obukhov phenomelogy, for $\ell > \ell_B$, buoyancy effects dominate the turbulent scaling relations and for $\ell < \ell_B$, turbulence dominates. Our simulations have enough resolution to resolve the Ozmidov length-scale ℓ_O within the inertial range of turbulence (i.e. see the top panel of Fig. 9; bottleneck effects dominate for $|k| \gtrsim 20$). But as shown in Alam, Guha & Verma (2019), $\ell_B \ll \ell_O$, and is difficult to resolve in numerical simulations with our setup. Although we do not observe a scaling transition within the same power spectrum (probably due to a lack of resolution), we observe a transition in the power spectrum slope at around Ri $\sim$ 1, which corresponds to $\ell_O \approx L_{\rm driv}$. This transition is even more evident in $P(\bar{\rho}_{k_z})$ and $P(\mathcal{M}_{k_z})$, and the corresponding ratios $R(\bar{\rho}_{k_{z,xy}})$ and $R(\mathcal{M}_{k_{z,xy}})$, which become steeper for Ri $\gtrsim 1$.

There is a major difference between our simulations and those in the above studies – the forcing field, we use has components along all three directions (both perpendicular and parallel to the stratification profile), whereas the others have components only perpendicular to the profile. The difference in driving is mainly because the above studies model the stratified turbulence in the earth's atmosphere and oceans, while we are motivated by the turbulence in the ICM, where driving by AGN jets is not limited to directions perpendicular to the stratification profile. In order to test the dependence of our results on the driving, we conducted two simulations (Ri0.6NV and Ri10NV; see Table 1) with turbulent driving only perpendicular to the stratification profile. We compare σ_s and α (slope of density power spectrum) of these runs to corresponding runs Ri0.5 and Ri13 which have isotropic driving. We find that σ_s and α for both these simulations lie within error bounds of each other (see Table 1 for α and σ_s). Even with 2D

[2]Note that, unlike here, in fig. 16 of Mohapatra & Sharma (2019), we define $\eta_k = (\delta\rho_k/ < \rho >)/(v_k/c_s)$ using the 3D velocity power spectrum.

forcing, due to Kelvin–Helmholtz instability, the flow breaks down into 3D turbulence and similar results are obtained for 2D and 3D forcing. Even with horizontal driving, we see significant anisotropy in both velocity and density fields only for Ri $\gtrsim 1$.

We propose a new relation between σ_s, $\mathcal{M}$, and Ri, where density fluctuations depend on Mach number, Richardson number, and the ratio of entropy and pressure scale heights ($\mathcal{M}$, Ri and H_S/H_P). But we have only exhaustively scanned the parameter space of Ri. Following up on this, it is important to test this relation for different values of all the three dimensionless numbers. We also need to extend the fitting function to Ri $\gtrsim 1$ (which is also relevant for clusters) and quantify the anisotropy in the velocity distribution.

For Ri $\gtrsim 1$ runs, we have large variations in Ri and temperature T along the stratification direction. This prevents us from conducting a simulation for a particular Ri and having uniform $\mathcal{M}$ throughout the box. For example, in our strongest stratification run Ri13, Ri increases from 3 to 30 and $\mathcal{M}$ decreases from 0.35 to 0.15 from $z = -0.5$ to $z = 0.5$ (due to variation in T). σ_s, which depends on both these parameters, increases from 0.18 at $z = -0.5$ to 0.24 at $z \approx -0.2$, reaches a peak and then decreases with increasing z to 0.1 at $z = 0.5$. The setup also prevents us from simulating highly stratified turbulence with Ri ~ 100, which should be around the upper limit of the strength of stratification for clusters.

Cooling and thermal instability, thermal conduction, and magnetic fields are some of the physics that are important for a realistic ICM and are not a part of this study. These effects can affect the density power spectrum, as seen in Gaspari et al. (2014) and Mohapatra & Sharma (2019). While conduction tries to eliminate density fluctuations and gradients, stratification, and cooling do quite the opposite. A parameter scan of different levels of cooling and thermal conduction and stratification will be an important study for the near future.

5 CONCLUSIONS

In this study, we have conducted idealized simulations of stratified turbulence with different levels of stratification using high-resolution hydrodynamic simulations. We have covered the parameter space $0.001 \lesssim$ Ri $\lesssim 10$. Ri ~ 1 is most relevant for modelling subsonic stratified turbulence in the ICM, which we have sampled with nine simulations (Table 1). The following are the main conclusions of our study:

(i) The amplitude of density fluctuations (denoted in log-scale by σ_s) is dependent on the Richardson number (Ri), and it increases with increasing Ri for Ri $\lesssim 10$. For weakly stratified subsonic turbulence (with Ri $\lesssim 1$, $\mathcal{M} < 1$), we derive a new relation $\sigma_s^2 = \ln(1 + b^2\mathcal{M}^4 + 0.09\mathcal{M}^2 \mathrm{Ri} H_P/H_S)$. Thus, we find that the density fluctuations in a weakly stratified medium (the last term in the previous expression) depend on three dimensionless parameters: $\mathcal{M}$, Ri, and H_P/H_S. For Ri $\gtrsim 10$, the magnitude of density fluctuations may become independent of Ri.

(ii) The amplitude of pressure fluctuations is independent of Ri for Ri $\lesssim 10$. For subsonic turbulence with Ri $\lesssim 10$, we show that $\sigma_{\ln(\bar{P})} = \ln(1 + b^2\gamma^2\mathcal{M}^4)$. This implies that thermal SZ fluctuations are easier to convert to velocity fluctuations as compared to X-ray SB fluctuations. This is also true in the presence of thermal instability, as discussed in Mohapatra & Sharma (2019).

(iii) Density fluctuations are predominantly adiabatic in homogeneous, isotropic, and unstratified turbulence. However, we find that they become increasingly isobaric in strongly stratified turbulence.

(iv) The 3D velocity power spectrum is mostly independent of Ri. However, binning along different **k** directions separately shows that $P(\mathcal{M}_{k_z})$ becomes steeper on increasing Ri beyond 1. Velocity component PDFs also show significant anisotropy for Ri $\gtrsim 1$.

(v) The power spectrum of density fluctuations $P(\bar{\rho}_k)$ varies both in amplitude and slope with Ri. The slope of the power spectrum α initially becomes shallower with Ri, peaks at around Ri ~ 1 and then becomes steeper again for Ri $\gtrsim 1$. This corresponds to anisotropy in turbulent eddies, becoming significant for Ri $\gtrsim 1$, where $L_{\rm driv} \approx \ell_O$ (the Ozmidov length-scale).

(vi) The normalized density ($\bar{\rho} = \rho/\langle\rho(z)\rangle$) distribution is close to lognormal.

(vii) We observe a positive correlation between $\delta\bar{\rho}$ and v_z in stratified turbulence, for $0.01 \lesssim$ Ri $\lesssim 1$, which reflects the conversion of kinetic energy into gravitational potential energy.

ACKNOWLEDGEMENTS

RM acknowledges helpful discussions with Eugene Churazov, Mahendra K. Verma, and Xun Shi for sharing data for Fig. 1. We thank the anonymous referee for helpful comments, which improved this work. RM thanks MPA Garching, SISSA Trieste, IUCAA Pune, and IISc Bangalore for enabling his visits. CF acknowledges funding provided by the Australian Research Council (Discovery Project DP170100603 and Future Fellowship FT180100495), and the Australia-Germany Joint Research Cooperation Scheme (UA-DAAD). PS acknowledges a Swarnajayanti Fellowship from the Department of Science and Technology, India (DST/SJF/PSA-03/2016-17), and a Humboldt fellowship for supporting his sabbatical stay at MPA Garching. We further acknowledge high-performance computing resources provided by the Leibniz Rechenzentrum and the Gauss Centre for Supercomputing (grants pr32lo, pr48pi, and GCS Large-scale project 10391), the Australian National Computational Infrastructure (grant ek9) in the framework of the National Computational Merit Allocation Scheme and the ANU Merit Allocation Scheme. The simulation software FLASH was in part developed by the DOE-supported Flash Center for Computational Science at the University of Chicago.

REFERENCES

Alam S., Guha A., Verma M. K., 2019, J. Fluid Mech., 875, 961
Aluie H., 2011, Phys. Rev. Lett., 106, 174502
Arévalo P., Churazov E., Zhuravleva I., Forman W. R., Jones C., 2016, ApJ, 818, 14
Balbus S. A., Soker N., 1990, ApJ, 357, 353
Banerjee S., Galtier S., 2013, Phys. Rev. E, 87, 013019
Banerjee S., Galtier S., 2014, J. Fluid Mech., 742, 230
Banerjee N., Sharma P., 2014, MNRAS, 443, 687
Bautz M. W. et al., 2009, PASJ, 61, 1117
Boldyrev S., Nordlund, Å., Padoan P., 2002, ApJ, 573, 678
Bolgiano R. J., 1962, J. Geophys. Res., 67, 3015
Bouchut F., Klingenberg C., Waagan K., 2007, Numer. Math., 108, 7
Bouchut F., Klingenberg C., Waagan K., 2010, Numer. Math., 115, 647
Brethouwer G., Lindborg E., 2008, Geophys. Res. Lett., 35, L06809
Brunetti G., Lazarian A., 2007, MNRAS, 378, 245
Carnevale G. F., Briscolini M., Orlandi P., 2001, J. Fluid Mech., 427, 205
Cavaliere A., Lapi A., Fusco-Femiano R., 2011, A&A, 525, A110
Choudhury P. P., Sharma P., Quataert E., 2019, MNRAS, 488, 3195
Churazov E., Sunyaev R., Forman W., Böhringer H., 2002, MNRAS, 332, 729
Churazov E., Forman W., Jones C., Böhringer H., 2003, ApJ, 590, 225
Churazov E., Arevalo P., Forman W., Jones C., Schekochihin A., Vikhlinin A., Zhuravleva I., 2016, MNRAS, 463, 1057

Corrsin S., 1951, J. Appl. Phys., 22, 469
Deusebio E., Vallgren A., Lindborg E., 2013, J. Fluid Mech., 720, 66
Dubey A. et al., 2008, in Pogorelov N. V., Audit E., Zank G. P., eds, ASP Conf. Ser. Vol. 385, Numerical Modelling of Space Plasma Flows. Astron. Soc. Pac., San Francisco, p. 145
Eswaran V., Pope S. B., 1988, Comput. Fluids, 16, 257
Federrath C., 2013, MNRAS, 436, 1245
Federrath C., Klessen R. S., Schmidt W., 2008, ApJ, 688, L79
Federrath C., Roman-Duval J., Klessen R. S., Schmidt W., Mac Low M. M., 2010, A&A, 512, A81
Fernando H. J. S., Hunt J. C. R., 1996, Dyn. Atmos. Oceans, 23, 35
Frisch U., 1995, Turbulence, Cambridge University Press, Cambridge, UK
Fryxell B. et al., 2000, ApJS, 131, 273
Galtier S., Banerjee S., 2011, Phys. Rev. Lett., 107, 134501
Gaspari M., Churazov E., 2013, A&A, 559, A78
Gaspari M., Ruszkowski M., Sharma P., 2012, ApJ, 746, 94
Gaspari M., Churazov E., Nagai D., Lau E. T., Zhuravleva I., 2014, A&A, 569, A67
George M. R., Fabian A. C., Sanders J. S., Young A. J., Russell H. R., 2009, MNRAS, 395, 657
Grete P., O'Shea B. W., Beckwith K., 2020, ApJ, 889, 19
Herring J. R., Kimura Y., 2013, Phys. Scr. Volume T, 155, 014031
Hitomi Collaboration, 2016, Nature, 535, 117
Hopkins P. F., 2013, MNRAS, 430, 1880
Khatri R., Gaspari M., 2016, MNRAS, 463, 655
Kolmogorov A. N., 1941, Akad. Nauk SSSR Dokl., 32, 16
Konstandin L., Girichidis P., Federrath C., Klessen R. S., 2012, ApJ, 761, 149
Kumar A., Chatterjee A. G., Verma M. K., 2014, Phys. Rev. E, 90, 023016
Lighthill J., 1978, Waves in Fluids, Cambridge University Press, Cambridge
Lindborg E., 2006, J. Fluid Mech., 550, 207
Mac Low M.-M., McCray R., 1988, ApJ, 324, 776
McCourt M., Parrish I. J., Sharma P., Quataert E., 2011, MNRAS, 413, 1295
Mohapatra R., Sharma P., 2019, MNRAS, 484, 4881
Mroczkowski T. et al., 2019, Space Sci. Rev., 215, 17
Nelson K., Rudd D. H., Shaw L., Nagai D., 2012, ApJ, 751, 121
Nelson K., Lau E. T., Nagai D., 2014, ApJ, 792, 25
Nolan C. A., Federrath C., Sutherland R. S., 2015, MNRAS, 451, 1380
Omma H., Binney J., Bryan G., Slyz A., 2004, MNRAS, 348, 1105
Parmentier V., Showman A. P., Lian Y., 2013, A&A, 558, A91
Passot T., Vázquez-Semadeni E., 1998, Phys. Rev. E, 58, 4501
Schmidt W., Hillebrandt W., Niemeyer J. C., 2006, Comput. Fluids, 35, 353
Schmidt W., Federrath C., Klessen R., 2008, Phys. Rev. Lett., 101, 194505
Schuecker P., Finoguenov A., Miniati F., Böhringer H., Briel U. G., 2004, A&A, 426, 387
She Z.-S., Leveque E., 1994, Phys. Rev. Lett., 72, 336
Shi X., Zhang C., 2019, MNRAS, 487, 1072
Simionescu A. et al., 2019, Space Sci. Rev., 215, 24
Stein R. F., 1967, Sol. Phys., 2, 385
Valdarnini R., 2019, ApJ, 874, 42
Verma M., 2018, Physics of Buoyant Flows. World Scientific, New Jersey
Waagan K., Federrath C., Klingenberg C., 2011, J. Comput. Phys., 230, 3331
Zeldovich Y. B., Sunyaev R. A., 1969, Ap&SS, 4, 301
Zhang C., Churazov E., Schekochihin A. A., 2018, MNRAS, 478, 4785
Zhuravleva I., Churazov E., Kravtsov A., Lau E. T., Nagai D., Sunyaev R., 2013, MNRAS, 428, 3274
Zhuravleva I. et al., 2014a, Nature, 515, 85
Zhuravleva I. et al., 2014b, ApJ, 788, L13
Zhuravleva I., Allen S. W., Mantz A., Werner N., 2018, ApJ, 865, 53

APPENDIX A

In Section 3.4, we showed that the density PDFs were lognormal except for a low density tail (see Fig. 5). Here, we show that the density PDF is convergent over three levels of resolution so the tail is not an effect of lack of numerical resolution.

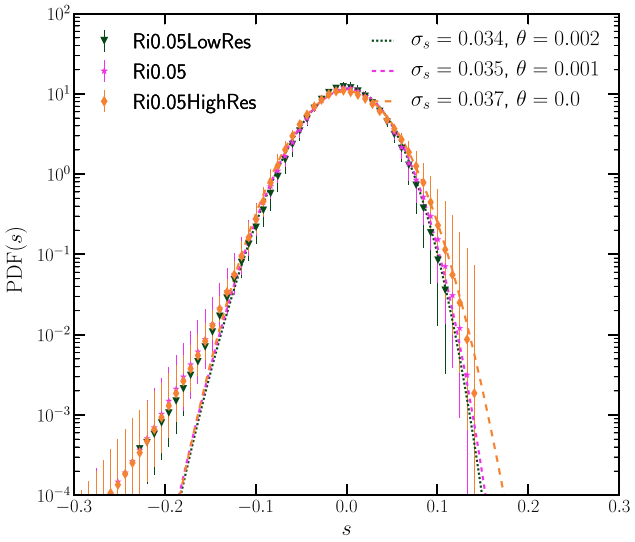

Figure A1. Volume weighted log-density PDF (similar to Fig. 5). The distributions are convergent for all three grid resolutions – $512^2 \times 768$, $1024^2 \times 1536$, and $2048^2 \times 3072$.

In the next plot, we justify our choice of $1024^2 \times 1536$ as the resolution for most of our simulations. From both upper and lower panel of Fig. A2, we can note that the spectral slopes of Ri0.05 and Ri0.05HighRes are convergent whereas Ri0.05LowRes gives us different slopes. Doubling the resolution gives us a longer inertial range but also consumes 16× more compute time. This plot shows that $1024^2 \times 1536$ has enough resolution to calculate velocity and density power spectra – as it gives the same slopes as the $2048^2 \times 3072$.

ADDITIONAL LINKS

An animation of the panels in Fig. 3 is available at this URL, https://www.youtube.com/watch?v = fYXbwO73Efc.

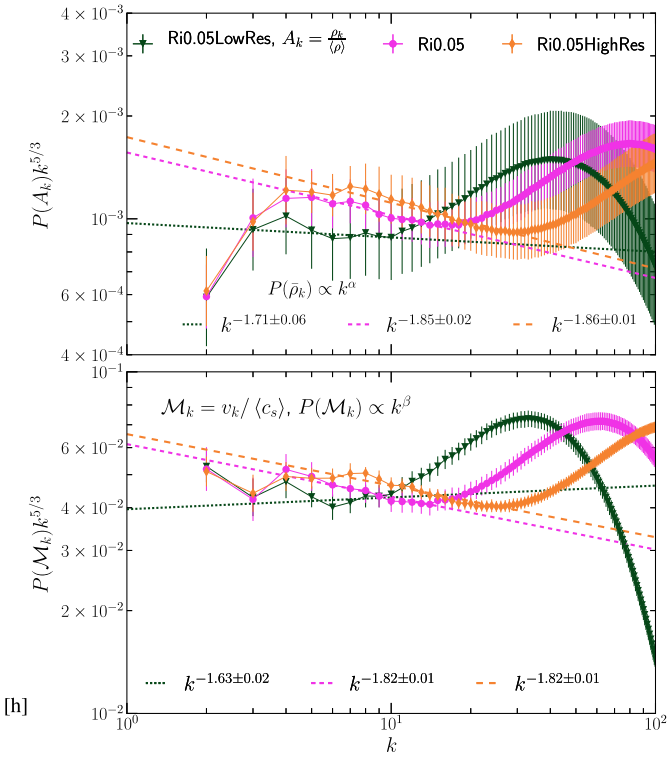

[h]

Figure A2. Compensated power spectra of $\bar{\rho}$ (upper panel) and $\mathcal{M}$ (lower panel) for different resolutions at Ri = 0.05. The slopes converge for Ri0.05 and Ri0.05HighRes. Ri0.1LowRes has insufficient inertial range.

This paper has been typeset from a TEX/LATEX file prepared by the author.